Consecutive extreme heat and flooding events in Argentina highlight the risk of managing increasingly frequent and intense hazards in a warming climate

Authors

Mariam Zachariah, Centre for Environmental Policy, Imperial College, London, UK
Juan Antonio Rivera, Instituto Argentino de Nivología, Glaciología y Ciencias Ambientales (IANIGLA), CCT CONICET Mendoza, Argentina.
Anna A. Sörensson, Facultad de Ciencias Exactas y Naturales, Universidad de Buenos Aires, Buenos Aires, Centro de Investigaciones del Mar y la Atmósfera,CONICET–Universidad de Buenos Aires, Buenos Aires, Argentina, CNRS–IRD–CONICET–UBA, Instituto Franco-Argentino para el Estudio del Clima y sus Impactos (IRL 3351 IFAECI), Buenos Aires, Argentina
Joyce Kimutai, Centre for Environmental Policy, Imperial College, London, UK
Ben Clarke, Centre for Environmental Policy, Imperial College, London, UK
Maja Vahlberg, Red Cross Red Crescent Climate Centre, The Hague, the Netherlands; Swedish Red Cross, Stockholm, Sweden (based in Ubmeje/Umeå, Sweden)
Karina Izquierdo, Red Cross Red Crescent Climate Centre (based in Mexico City, Mexico)
Emmanuel Raju, Copenhagen Centre for Disaster Research, Global Health Section, Department of Public Health, University of Copenhagen, Copenhagen, Denmark; African Centre for Disaster Studies, North-West University, South Africa
Nick Baumgart, Copenhagen Centre for Disaster Research, Global Health Section, Department of Public Health, University of Copenhagen, Copenhagen, Denmark
Friederike Otto, Centre for Environmental Policy, Imperial College, London, UK

Review authors

Sjoukje Philip, Royal Netherlands Meteorological Institute (KNMI), De Bilt, The Netherlands
Ben Clarke, Centre for Environmental Policy, Imperial College, London, UK
Roop Singh, Red Cross Red Crescent Climate Centre, The Hague, The Netherlands (based in New Jersey, USA)
Pablo Bruno, Argentine Red Cross, Buenos Aires, Argentina
Mercedes del C. Vega, Argentine Red Cross, Buenos Aires, Argentina
Tomás Matías Sarkis Badola, Argentine Red Cross, Buenos Aires, Argentina
Virginia Laino, Southern Cone Cluster, International Federation of Red Cross and Red Crescent Societies (IFRC), Buenos Aires, Argentina
Alejandro Orozco, Southern Cone Cluster, International Federation of Red Cross and Red Crescent Societies (IFRC), Buenos Aires, Argentina

Main findings

- In Northern Argentina, including the Buenos Aires province and CABA, intensified and more frequent extreme heat and heavy rainfall events as well as simultaneous or sequential extremes like heat-heavy rainfall or hot-dry events heighten the risk of compounding hydrometeorological hazards. CABA's aging population, urban development, and high population density increase both exposure and vulnerability to these hazards.
- Almost 50% of the urban population is employed in the informal economy and a large proportion of the urban livelihoods are sensitive to climate shocks e.g. due to employment disruption and exposure to heat.
- Based on gridded reanalysis products, we find that the extreme heat event is relatively rare, expected to occur in today's climate about once every 50 to 100 years. However, in a 1.3°C cooler climate, extreme heat such as observed in the summer 2024/25 would have been virtually impossible. When repeating the analysis for the shorter hot and humid heat wave directly preceding the rainfall event, we find a similarly large role of human-induced climate change.
- Climate models also show that climate change is making such temperatures much more frequent and intense. However, the increase in the models is smaller than in reanalysis products and thus likely underestimating the effect of climate change. Nevertheless, looking at the future, models show a very strong trend that increases with future warming, rendering such an event a common occurrence in a 2.6°C warmer climate compared to pre-industrial.
- The influence of climate change on the rainfall event is much less clear. While all of the 35 available weather stations in the area show an increase in the intensity of heavy rainfall of between 7-30% associated with global warming of 1.3°C, this is not represented in any of the available gridded reanalysis products which show on average a decreasing trend.
- Climate models are largely in agreement with the station data and on average show an increase in the likelihood and intensity of heavy rainfall such as observed in early March. A similar increase in most, but not all, models is seen for an additional 1.3°C warming, representing a 2.6°C climate.
- Station data and model data both show an increasing trend in extreme rainfall with rising temperatures, which is also what is expected for rainfall events of this kind in a warming climate. Thus, it is likely that climate change increased the likelihood and intensity of the heavy rainfall. However as station data and gridded data do not agree on the sign of the trend we cannot reconcile the two and make a conclusive statement.
- These consecutive events highlight the broader challenges of managing increasingly frequent and intense hazards in the province, where vulnerabilities are shaped by urbanization, infrastructure inadequacies, and social inequalities.
- As extreme weather events become more common, it is important to keep investing in early warning systems, climate-smart urban planning, and preparedness that takes multiple hazards into account. For instance, creating more green and blue spaces can help reduce heat in cities, provide relief during hot weather, and lower the risk of flooding—all of which can be done even in crowded urban areas.

1 Introduction

On the 7th of March 2025, the city of Bahía Blanca, Argentina, witnessed exceptionally extreme rainfall of more than 300 mm within only 8 hours. This amount is unprecedented in the observed meteorological records of the city (1956-2025), and represents almost half of the total annual precipitation according to the 1991-2020 climatology (639 mm). The event occurred in the context of several days of hot weather and high atmospheric humidity and was triggered by a cold front that remained quasi-stationary during the duration of the event, causing a cloudburst that flooded the city and surrounding areas. One week prior to the event, Bahía Blanca had recorded over 80 mm of rainfall, a factor that may have conditioned the saturation of the soil prior to the flooding event. The persistent extreme heat over Southern South America during summer 2025 led to the release of four special reports for heatwaves in Argentina, with 48 days of the season characterized by extreme temperatures (SMN Argentina, 2025a). Similar conditions were observed during the summer season over Uruguay (INUMET, 2025a) and Brazil (INMET, 2025a). Particularly, since the second half of February 2025, the extreme heat has led to temperatures above 40°C over northern Argentina, southern Brazil and much of Paraguay and Uruguay (NASA, 2025), with anomalies up to 10°C above average (The Guardian, 2025). Sixty one cities in central-north Argentina recorded heatwave conditions between 19th February to 8th March 2025, with maximum temperatures up to 43.3°C in Resistencia and minimum temperatures up to 30.4°C in Catamarca (SMN Argentina, 2025b).

The early warning system of the National Weather Service (SMN) of Argentina anticipated the magnitude of the rainfall event 48 hours before its occurrence, issuing a yellow warning (issued for > 40 mm in 12 hours) on March 5, which was upgraded to orange warning (issued for > 80 mm in 12 hours) on March 6. Considering this information, local authorities suspended outdoor activities and ordered school closures for March 7. During the first hours of the event, taking into account the rainfall rates over Bahía Blanca and surrounding areas, the SMN issued a red warning, which represents that more than 175 mm of precipitation is expected in 24 hours (Saucedo et al., 2023). Extreme heat warnings had been issued since January by all the meteorological services from Southern South America. The most prolonged heat period started on February 19, issued as moderate to extreme by the SMN and covering the region from northern Patagonia to the northern portion of Argentina (SMN Argentina, 2025b), while Brazil's National Institute of Meteorology (INMET) issued orange to red heat wave warnings for the central-southern portions of the country during late February and the first week of March 2025 (INMET, 2025b). In Uruguay, February 2025 was the warmest since 1981, with several locations exceeding 40°C (INUMET, 2025b), while in Paraguay 18 stations recorded heatwave conditions up to 10 days long (Dirección de Meteorología e Hidrología, 2025).

The storm and floods devastated the region, hitting Bahía Blanca hardest with fatalities, destruction, and hundreds left homeless (VOA News, 2025). The extreme rainfall affected over 300,000 people, with 16 reported deaths, 1,400 being displaced (A24, 2025) and two persons remaining missing two weeks after the event (La Nación, 2025). Critical infrastructure was damaged, leading to electricity outages, restricted access, and the evacuation of Jose Penna hospital (WIO News, 2025, News central, 2025, Earth Observatory, 2025). Bahía Blanca is located in the lower basin of the Napostá Grande creek, whose watercourse crosses the urban area in a north-south direction (Lambrecht and Zapperi, 2024). Part of the stream is diverted to the Maldonado channel, key for the storm drainage system of the city. The increase in the water levels affected river embankments and road infrastructure,

damaging several bridges that isolated Bahía Blanca after the flooding (Gobierno de la Provincia de Buenos Aires, 2025). The floods diminished the transportation of natural gas through the pipeline connecting Patagonia with Buenos Aires city, leading to energy supply issues in remote areas (El Economista, 2025). The port of Bahía Blanca is crucial for Argentina's maritime trade, especially for the export of grains and other products. Rail access to the port is completely cut off due to damage to the tracks. This represents considerable economic losses and a large investment to restore access. Approximately 100,000 trucks per day would be needed to replace the goods, especially grains, currently transported by rail to the port (Bianco, 2025). Another economic impact is that of oil refining, which is one of the region's key industrial sectors. The petrochemical hub remains with 50% of its operations inactive, and small and medium-sized enterprises (SMEs) have suffered economic losses due to damage to industrial facilities. The damage estimated in the city amounts to $ 400 million dollars (Ámbito, 2025). At the same time, heat alerts were issued in 15 provinces, with record temperatures in the north (Buenos Aires Herald, 2025, SMN Argentina via X). Buenos Aires faced blackouts and traffic disruptions affecting hundreds of thousands due to peak energy demand (Global Times, 2025, AP News, 2025). While no data on heat-related mortality is available, past events have shown increased mortality risks (Chesini et al., 2019; Chesini et al., 2021, Pinotti et al., 2024).

The rainfall event was caused by the interaction between the advance of a cold front and the presence of an unstable, warm and moist air mass that persisted during several days over much of Southern South America. Frontal passages during late summer and early autumn are a common climatic feature over the region (Oliveira et al., 2024), but the anomalous hot weather and high atmospheric humidity promoted the severity of the rainfall event. During the period between 1-6 March the occurrence of thunderstorms over much of the Pampas region was favoured by atmospheric instability, with convective available potential energy (CAPE) up to 4000 J/kg (SMN Argentina, 2025c). These high CAPE values and low-level moisture conditions are often associated with the presence of a low-level jet that transports heat and moisture from the Amazon towards the Pampas region (Oliveira et al., 2018). The moisture transport was promoted by an strengthened South Atlantic semi-permanent anticyclone, located further westward than its normal position, covering part of Southern South America (Figure 1). This synoptic configuration also promoted the persistence of warm anomalies over much of Southern South America, typically linked to positive Z500 anomalies (Suli et al., 2023). The role of drylines to initiate and organize deep convection prior to the flooding event is apparent, given the marked contrast in atmospheric humidity between the moist air mass over the Pampas region and the dry air mass over Northern Patagonia (Bechis et al., 2020). An intense mid-tropospheric trough (Figure 1) with an associated cold front, oriented from north-west to south-east, slowly moved towards the northeast of Argentina between 6 and 7 of March, triggering the cloudburst over Bahía Blanca city and surrounding areas, where soils were close to saturation due to preceding rainfall accumulation.

Extreme rainfall events over Bahía Blanca and surrounding areas tend to occur mainly during the months of spring and summer, where the main impacts are related to the occurrence of floods and even tornadoes (Rasmussen et al., 2014). The city often reports impacts when daily precipitation is above 20 mm (Lambrecht and Zapperi, 2024), highlighting that its infrastructure is not prepared to face an increasing frequency of precipitation extremes over the region. The interannual variability of daily precipitation extremes is linked with El Niño–Southern Oscillation and the Indian Ocean Dipole, while decadal variability is associated with the Atlantic Multi-decadal Oscillation (Robledo et al., 2020).

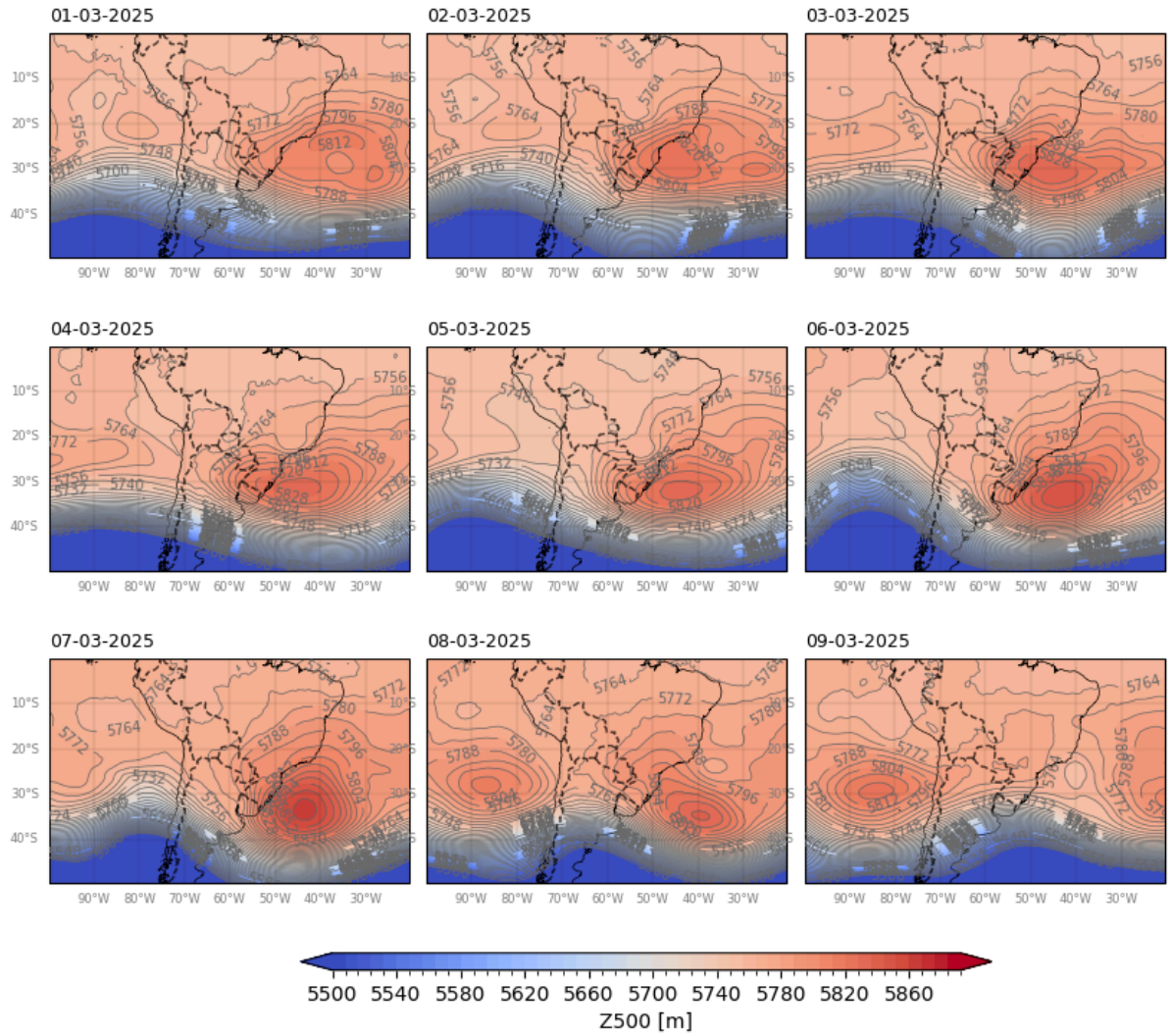

Figure 1 Geopotential height at 500hPa during the period of the event. Data: ERA5

1.1 Rainfall and heat extremes in Southern South America

Although some regions are getting dryer and others wetter in terms of annual mean precipitation with anthropogenic climate change, according to the latest Synthesis Report of IPCC (IPCC 2023), extreme rainfall, when it occurs, is increasing in intensity over all land-regions worldwide. This is the case of Southern South America, where several extreme precipitation indices showed positive trends over the last 50 years (Penalba and Robledo, 2010; Cerón et al., 2021). Bahía Blanca experienced a severe storm during 16th December 2023, with 60 mm of rainfall and wind gusts of more than 150 km/h, resulting in 13 fatalities (Lambrecht et al., 2024). In this region, a large part of the floodings produced by extreme precipitation occurs in low-lying riverside cities, such as the pluvial flooding in La Plata in 2013 (Etulain and López, 2017), where 313mm in only 6 hours caused 89 official fatalities. The Buenos Aires metropolitan area recorded more than 120 mm of rain during 12th March 2024, leading to public transport disruptions, flight delays, and hundreds of cars underwater (Floodlist, 2025).

Human-induced climate change has increased the frequency and severity of extreme heat events globally, with adverse impacts on human health, livelihoods and infrastructure, particularly in urban areas (IPCC 2023). Southern South America experienced an increase in the intensity and frequency of extreme temperature indicators over the last half century (Geirinhas et al., 2018; Olmo et al., 2020; González-Reyes et al., 2023), with some regions reporting a parallel increment in the occurrence of droughts and fire weather conditions (Feron et al., 2024). The extreme heat during the 2022/23 season in Argentina caused the largest number of heatwaves in the last 60 years, with temperatures up to 46°C (Collazo et al., 2024; Rivera et al., 2023). The unusual heatwave of early spring 2020 in Central South America led to temperatures up to 10°C above normal, with maximum temperatures over 40°C in Paraguay and Central Brazil (Marengo et al., 2021). Several studies documented that human-caused climate change increased the likelihood and severity of most of these extreme heat events (Collazo et al., 2024; Kew et al., 2023; Rivera et al., 2023), with increased mortality linked to the record-breaking temperatures (Collazo et al., 2025). On the other hand, few event attribution studies focused on the evaluation of extreme rainfall events in Southern South America, most of them considered case studies from Brazil (Clarke et al., 2024; Junior et al., 2024). These studies showed that human-induced climate change increased both the likelihood and the intensity of heavy rainfall. Process-based studies have however linked the increase in summer mean precipitation and in extreme precipitation during summer over Southeastern South America to anthropogenic climate change (Doblas-Reyes et al. 2021).

1.2 Event Definition

The multiple hot spells that hit Southern South America, including the notable heatwave around 17th February, witnessed temperature records being broken at several locations in Argentina and the neighbouring countries of Paraguay, Uruguay and Brazil during the peak summer month of February (MercoPress, 3 Feb 2023; Earth Observatory, NASA). In the days leading to the extreme rainfall in Bahía Blanca on the 7th of March that brought about the devastating floods, the last of these hot spells coincided with the air masses that were responsible for the extreme rainfall, causing warm and moist conditions that led to both elevated thermal discomfort levels and rains in neighbouring regions. In this study, we conduct event attribution analyses of both the extreme rainfall event and the exceptionally warm summer months that witnessed the multiple hot spells. Additionally, using a gridded reanalysis dataset, we analyse the trends in the heat index over the region during the last of the heatwaves that reportedly began around the 18th of February and persisted till the heavy rainfall on the 7th of March.

For the rainfall event, we choose the 7-day rainfall from the 1st of March to the 7th when the downpours occurred in Bahía Blanca. For the spatial extent, we choose the provinces which were under orange to red alert on the 7th. Fig. 1.2 (a) shows the rainfall during 1-7 March, with the study region highlighted in red. The region comprises the provinces of Buenos Aires, La Pampa, Córdoba and San Luis. For the heat event, we focus on the summer seasonal (DJFM) mean of the daily maximum temperature, given that there were at least two recorded heat waves since the beginning of February and the first days of March. We chose the IPCC's South East South America domain (SES) as the study region to capture the spread of the event and to facilitate comparison to literature. Fig. 1.2(b) shows the study region. Fig. 1.2 (c) shows the average heat index over the same region during 21 days from 15 February- 7 March 2025, when the last and the most prolonged heatwave occurred.

We use the National Oceanic and Atmospheric Administration (NOAA) operational Heat Index (HI). The HI during this period corresponds to 'caution' to 'extreme caution' levels, which is associated with increasing risk of heat strokes, cramps and exhaustion under prolonged exposure (NOAA; see Fig. A1).

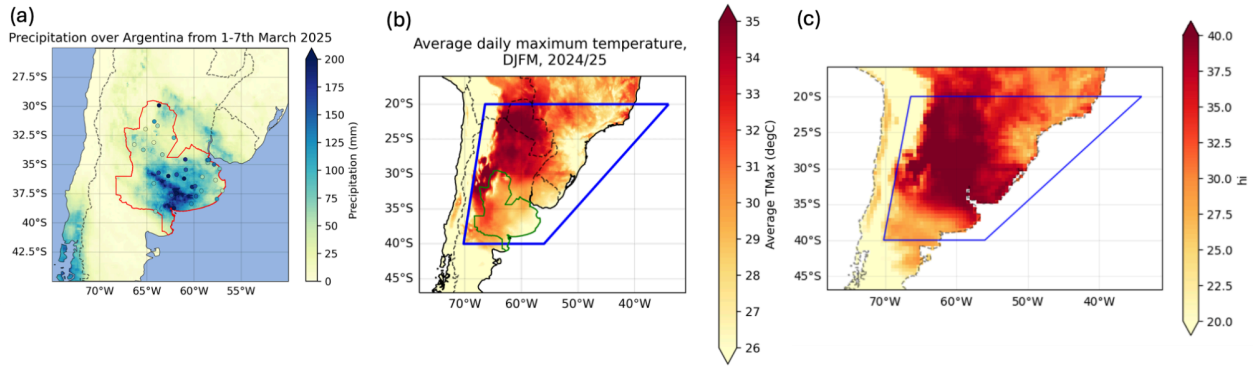

Figure 1.2(a): 7-day accumulated rainfall during 1-7 March 2025, based on MSWEP data. The study region is highlighted in red. The scatter plots show the rainfall accumulations for the same period from 25 weather stations by the National Weather Service of Argentina (NWS). (b) The average of daily maximum temperature during 1 Dec 2025 -18 March 2025, based on MSWX dataset. The study region (South East South America domain or the SES domain) is highlighted in blue. (c) Average Heat index (HI) during 15 Feb-7 March, 2025, based on ERA5 dataset. The blue highlight shows the SES domain.

In this report, we study the influence of anthropogenic climate change by comparing the likelihood and intensity of similar extreme rainfall events and hot summers at present with those in a 1.3 °C cooler climate. We also extend this analysis into the future by assessing the influence of a further 1.3 °C of global warming from present. This is in line with the latest Emissions Gap Report from the United Nations Environment Programme, which shows that the world is on track for at least 2.6 °C temperature rise given currently implemented policies (UNEP, 2024).

2 Data and methods

2.1 Observational data

A range of observational and reanalysis datasets are used in this study to evaluate changes in extremes in the historical record with warming. These are as follows:

1. **ERA5 (daily precipitation, daily maximum temperature)** - The European Centre for Medium-Range Weather Forecasts's 5th generation reanalysis product, ERA5, is a gridded dataset that combines historical observations into global estimates using advanced modelling and data assimilation systems (Hersbach et al., 2020). We use daily precipitation and daily maximum temperature data from this product at a resolution of 0.5°×0.5°, from the years 1950 to present.
2. **MSWX (daily maximum temperature)** - The Multi-Source Weather, MSWX, dataset (Beck et al., 2022), which combines various observational and reanalysis-based data for reliable

bias-corrected weather variable estimates, at 3-hourly intervals from 1979 to near real-time, and at 0.1° spatial resolution globally.

3. **MSWEP (daily precipitation)** - The Multi-Source Weighted-Ensemble Precipitation (MSWEP) v2.8 dataset (updated from Beck et al., 2019) is fully global, available at 3-hourly intervals and at 0.1° spatial resolution, available from 1979 to ~3 hours from real-time. This product combines gauge-, satellite-, and reanalysis-based data.
4. **CPC (daily precipitation, daily maximum temperature)** - This is the gridded product from NOAA PSL, Boulder, Colorado, USA known as the CPC Global Unified Daily Gridded data, available at 0.5° x 0.5° resolution, for the period 1979-present. Data are available from NOAA.
5. **CHIRPS (daily precipitation)** - The rainfall product developed by the UC Santa Barbara Climate Hazards Group called "Climate Hazards Group InfraRed Precipitation with Station data" (CHIRPS; Funk et al. 2015). Daily data are available at 0.05° resolution, from 1981-28 February 2025. The product incorporates satellite imagery with in-situ station data.
6. **Meteorological Stations** - Time series of daily rainfall from January 1961 to March 13th 2025 at the locations shown in Figure 1.2 were used to evaluate local trends in return times. These station data were provided by Argentina's National Weather Service. The selected stations cover the provinces which were under orange to red alert on March 7th.

Finally, as a measure of anthropogenic climate change we use the (low-pass filtered) global mean surface temperature (GMST), where GMST is taken from the National Aeronautics and Space Administration (NASA) Goddard Institute for Space Science (GISS) surface temperature analysis (GISTEMP, Hansen et al., 2010 and Lenssen et al. 2019).

2.2 Model and experiment descriptions

Across the two event definitions, we use 2 multi-model ensembles from climate modelling experiments using very different framings (Philip et al., 2020): Sea Surface temperature (SST) driven global circulation high resolution models and regional climate models.

1. Coordinated Regional Climate Downscaling Experiment CORDEX-CORE (11 models with at 0.44° resolution (SAM-44) and 5 models at 0.22° resolution (SAM-22)) multi-model ensemble (Giorgi and Gutowski, 2015; Giorgi et al., 2021), comprising 14 simulations resulting from pairings of Global Climate Models (GCMs) and Regional Climate Models (RCMs)). These simulations are composed of historical simulations up to 2005, and extended to the year 2100 using the RCP8.5 scenario. We use daily precipitation from this ensemble.
2. HighResMIP SST-forced model ensemble (Haarsma et al. 2016), the simulations for which span from 1950 to 2050. 15 models are used in this study. The SST and sea ice forcings for the period 1950-2014 are obtained from the 0.25° x 0.25° Hadley Centre Global Sea Ice and Sea Surface Temperature dataset that have undergone area-weighted regridding to match the climate model resolution (see Table B). For the 'future' time period (2015-2050), SST/sea-ice data are derived from RCP8.5 (CMIP5) data, and combined with greenhouse gas forcings from SSP5-8.5 (CMIP6) simulations (see Section 3.3 of Haarsma et al. 2016 for further details). We use both daily precipitation and maximum temperature from this ensemble.

2.3 Statistical methods

Methods for observational and model analysis and for model evaluation and synthesis are used according to the World Weather Attribution Protocol, described in Philip et al., (2020), with supporting details found in van Oldenborgh et al., (2021), Ciavarella et al., (2021), Otto et al., (2024) and here. The key steps, presented in sections 3-6, are: (3) trend estimation from observations; (4) model validation; (5) multi-method multi-model attribution; and (6) synthesis of the attribution statement.

In this report we analyse time series of annual (July-June) maximum 7-day accumulated precipitation over the region that were under orange or red warning, and December-March mean of daily maximum temperature over the wider Southeastern South America region.

A nonstationary generalised extreme value (GEV) distribution is used to model the extreme 7-day precipitation (RX7day), and a nonstationary normal distribution is used to model the seasonal temperature. For precipitation, the distribution is assumed to scale exponentially with the covariate, with the dispersion (the ratio between the standard deviation and the mean) remaining constant over time; while for temperatures, the distribution is assumed to shift linearly with the covariate, while the variance remains constant. The parameters of the statistical model are estimated using maximum likelihood. Including a measure of Nino3.4 as a second covariate in the precipitation fitting did not improve the fits, so this is not considered further.

For each time series we calculate the return period and intensity of the event under study for the 2024 GMST and for 1.3 C cooler GMST: this allows us to compare the climate of now and of the preindustrial past (1850-1900, based on the Global Warming Index), by calculating the probability ratio (PR; the factor-change in the event's probability) and change in intensity of the event.

3 Observational analysis: return period and trend

3.1 Analysis of point station data and gridded data

Table 3.1 summarises the magnitude of the extreme rainfall and the seasonal average of the daily-maximum temperature in 2025, area-averaged over the respective study regions, along with the estimated return periods in the 2025 climate.

For the extreme rainfall event- annual (Jul-Jun) RX7day, these estimates come from four gridded datasets- ERA5, MSWEP, CPC and CHIRPS, area-averaged over the study region (see section 1.2) and based on rainfall averaged over 25 stations in the study region. It should be noted that CHIRPS did not have the event at the time of writing this report, and a return period of 50 years was used to analyse the event. The magnitude of the 2025 event is the highest in the station-average at 122.8mm, with a return period of 51 years (95% uncertainty interval: 13 to inf). In the three gridded datasets which have data covering the event, the event is not as rare with return periods ranging from ~3 to 15 years. Ground reports of the event state that the extreme rainfall event over Bahía Blanca to have been

the worst floods in decades. Therefore, for the model analysis we use a rounded value of 50 years estimated from the station analysis.

The magnitude and return period of the seasonal average of daily maximum temperature (avgTMax_DJFM), area-averaged over the SES region is estimated from three gridded datasets- ERA5, MSWX and CPC. The magnitude of the event is the same for the MSWX and ERA5 datasets at about 28.7℃. However, it is a rare event in the longer ERA5 dataset, having a return period of 121 years in the current climate, whereas a much less extreme 1 -in-30 year event in the MSWX data. Although the CPC dataset has consistently higher temperatures with a magnitude of 31.15℃ for the 2025 TMax_DJFM, the return period of 24 years which is close to that estimated based on MSWX data. For the model analysis, we use a rounded value of 50 years.

Dataset	7-day extreme precipitation		December-March seasonal temperature	
	Magnitude (mm)	Return period (95% C.I.)	Magnitude (°C)	Return period (95% C.I.)
ERA5	66.26	2.55 (1.66 - 5.69)	28.71	120.76 (24.8 - 3048.78)
MSWEP	75.97	9.80 (3.93 - 44.71)		
MSWX			28.70	29.8 (7.54 - 639.34)
CPC	88.34	15.92 (5.17 - 396.18)	31.15	23.76 (6.39 - 424.08)
CHIRPS	82.132	50		
Stations	122.8	51.18 (12.49 - inf)		

Table 3.1: Estimated return periods of RX7day over the study region (Fig 1.2, left) and TMax_DJFM over the SES region (Fig 1.2, right) in the 6 observational and reanalysis datasets.

The left panels in Fig. A2 shows the trends in time series of annual (Jul-Jun) rx7day over the study region associated with GMST in the gridded datasets and station averaged over the region. While the station average shows an overall increasing response to increase in global mean temperatures, the time series derived from the gridded datasets are found to show a decreasing trend in response to warming. The right panels in Fig. S1 shows the return period curves for the climate of today and a hypothetical, pre-industrial climate that would have been 1.3℃ cooler climate. Compared to the preindustrial climate, the current warming level has resulted in a decrease in the likelihood of extreme rainfall events such as the one under study by a factor of 0.67, 0.37, 0.57 and 0.4 based on the ERA5, MSWEP, CPC and CHIRPS datasets, respectively (see Table 3.2). Following from this, there is an estimated 6.4% to 11.4% decrease in the rainfall amount based on the gridded datasets, albeit with large uncertainties. On the other hand, the return period curves based on the station-averaged rainfall

shows a tripling in the likelihood of extreme rainfall spells along with a 9% increase in the rainfall amounts, as compared to the pre-industrial climate. This increasing tendency in the station -average is a result of independent stations in the region showing similar trends. Table A1 shows the results from analysing the trends at stations in five locations in the study region- namely, Bahía Blanca, Dolores, Santa Rosa, Bolívar and Córdoba (see Appendix Fig. A3 for the locations of these stations), which all suggest that extreme rainfall in the region is increasing in response to global warming.

Dataset	Trend due to GMST : RX7day	
	Probability Ratio	Change in magnitude (%)
ERA5	0.67 (0.25 - 1.32)	-10.54 (-28.4 - 8.89)
MSWEP	0.37 (0.051 - 2.98)	-15.76 (-41.04 - 21.41)
CPC	0.57 (0.013 - 155.57)	-6.43 (-40.35 - 35.99)
CHIRPS	0.30 (0.04 - 6.20)	-11.36 (-31.40 - 21.96)
Stations	3.33 (10^{-5} - inf)	8.98 (-16.04 - 39.58)

Table 3.2: Change in probability and magnitude for RX7day in the study region due to both GMST. Boxes shaded in blue indicate an increasing trend and boxes shaded in orange indicate a decreasing trend. Trends that are statistically significant are highlighted in bold text.

Fig. A4 shows the trends and the return period curves associated with GMST levels for the seasonal (DJFM) average of daily maximum temperature for the SES domain. The direction of change in the seasonal temperatures is as expected and consistent across the three datasets-ERA5, MSWX and CPC, all showing an increasing tendency associated with global warming, at different rates. Once again, ERA5 and MSWX are comparable, showing an increase of 1.39℃ and 1.84℃ associated with a global warming of 1.3℃. The CPC shows a much steeper increase of 2.5℃. The PR values are very high across all datasets suggesting that the anomalously high seasonal temperature during this year would have been virtually impossible without human-induced climate change.

Dataset	Trend due to GMST : DJFM TMax	
	Probability Ratio	Change in magnitude (℃)
ERA5	**7.80E+07** **(6.04E+05 - 1.55E+11)**	**1.39** **(1.04 - 1.71)**
MSWX	**2.33E+10** **(5.36E+06 - 9.72E+18)**	**1.84** **(1.25 - 2.48)**
CPC	**3.95E+10** **(6.93E+06 - 4.15E+18)**	**2.47** **(1.67 - 3.26)**

Table 3.3: Change in probability and magnitude for seasonal temperature in Southeastern South America (SES) due to GMST. Boxes shaded in blue indicate an increasing trend. Trends that are statistically significant are highlighted in bold text.

In addition to the summer season being unusually hot in the SES region, in the days leading to the extreme rainfall spell on the 7th March, the high temperatures were accompanied by high humidity. To understand whether there is a discernible trend associated with GMST in the combined hot and humid conditions, using only ERA5 dataset, we calculated the Heat Index (see WWA, South Asia Heatwave , 2023; WWA, West Africa Heatwave, 2024) and repeat the above analysis for the annual (July-June) 21-day average HI, area-averaged over the SES region. Appendix Fig. A5 shows the trend in the time series associated with GMST and the return period curves. This year's event, which is found to have a return period of about 20 years in today's climate, would have been virtually impossible in the pre-industrial climate (Table 3.4), as evident from the Probability Ratio which tends to inf (uncertainty: 207 to inf). The intensity changes show that climate change has made the event 2°C hotter (uncertainty: 1.18°C to 2.66°C) as compared to a 20-year humid heat event in the pre-industrial climate.

Dataset	Trend due to GMST : 21-day Heat Index	
	Probability Ratio	Change in magnitude (℃)
ERA5	**Inf (2.07 - inf)**	**2.0 (1.18 - 2.66)**

Table 3.4: Change in probability and magnitude for 21-day Heat Index in Southeastern South America (SES) due to GMST in ERA5. Boxes shaded in blue indicate an increasing trend. Trends that are statistically significant are highlighted in bold text.

4 Model evaluation

In this section we show the results of the model evaluation for the assessed region. The climate models are evaluated against the observations in their ability to capture:

1. **Seasonal cycles**: For this, we qualitatively compare the seasonal cycles based on model outputs against observations-based cycles. We discard the models that exhibit ill-defined peaks in their seasonal cycles. We also discard the model if the rainy season onset/termination varies significantly from the observations.

2. **Spatial patterns**: Models that do not match the observations in terms of the large-scale precipitation patterns are excluded.

3. **Parameters of the fitted statistical models.** We discard the model if the model and observation parameters ranges do not overlap.

The models are labelled as ‘good’,’reasonable’, or ’bad’ based on their performances in terms of the three criteria discussed above. A model is given an overall rating of ‘good’ if it is rated ‘good’ for all three characteristics. If there is at least one ‘reasonable’, then its overall rating will be ‘reasonable’ and ‘bad’ if there is at least one ‘bad’.

We only use models with the label 'good’, as there are more than five models per framing that perform well according to our evaluation tests. The tables show the model validation results.

4.1 Annual (July-June) RX7day over the Orange Alert region

The table showing evaluation values. For large multi-models only show models that passed the evaluation test and show an extended table at the bottom of the document.

Table 4.1 Evaluation results of the climate models considered for attribution analysis of RX7day over the Orange Alert study region. For each model, the threshold for a 1-in-50-year event is shown, as well as the best estimates of the Dispersion and Shape parameters, along with 95% confidence intervals. Furthermore evaluation of the seasonal cycle and spatial pattern are shown.

Model / Observations	**Seasonal cycle**	**Spatial pattern**	**Dispersion**	**Shape parameter**	**Conclusion**
MSWEP			0.199 (0.139 ... 0.234)	0.033 (-0.24 ... 0.42)	
CPC			0.205 (0.152 ... 0.241)	-0.098 (-0.46 ... 0.21)	
ERA5			0.229 (0.177 ... 0.268)	-0.21 (-0.48 ... -0.014)	
CHIRPS			0.154 (0.0954 ... 0.179)	-0.018 (-0.31 ... 0.44)	
Stations			0.220 (0.173 ... 0.257)	-0.13 (-0.35 ... 0.032)	
CORDEX					
CanESM2_SMHI-RCA4 historical-rcp85	good	good	0.269 (0.219 ... 0.308)	-0.22 (-0.36 ... -0.092)	reasonable
CanESM2_UCAN-WRF341I historical-rcp86	good	good	0.249 (0.201 ... 0.287)	-0.098 (-0.26 ... 0.068)	good
CNRM-CM5_SMHI-RCA4 historical-rcp87	reasonable	bad	0.250 (0.208 ... 0.287)	-0.028 (-0.29 ... 0.12)	bad
CSIRO-Mk3-6-0_SMHI-RCA4 historical-rcp88	good	good	0.250 (0.211 ... 0.283)	-0.13 (-0.35 ... 0.13)	good
EC-EARTH_SMHI-RCA4 historical-rcp89	bad	bad	0.286 (0.235 ... 0.327)	-0.12 (-0.33 ... 0.064)	bad
GFDL-ESM2M_SMHI-RCA4 historical-rcp90	good	good	0.254 (0.190 ... 0.299)	0.061 (-0.087 ... 0.30)	good
HadGEM2-ES_CTP-RegCM4-7 historical-rcp91	good	good	0.213 (0.163 ... 0.250)	-0.091 (-0.48 ... 0.20)	good
HadGEM2-ES_GERICS-REMO2015 historical-rcp92	good	good	0.200 (0.159 ... 0.232)	0.059 (-0.27 ... 0.27)	good

HadGEM2-ES_ICTP-RegCM4-3 historical-rcp93	good	good	0.256 (0.183 ... 0.305)	-0.027 (-0.31 ... 0.26)	good
HadGEM2-ES_SMHI-RCA4 historical-rcp94	good	good	0.215 (0.172 ... 0.250)	-0.0035 (-0.14 ... 0.15)	good
IPSL-CM5A-MR_SMHI-RCA4 historical-rcp95	good	good	0.229 (0.193 ... 0.256)	-0.14 (-0.36 ... 0.059)	good
MIROC5_SMHI-RCA4 historical-rcp96	good	good	0.224 (0.176 ... 0.260)	-0.12 (-0.25 ... 0.058)	good
MPI-ESM-LR_GERICS-REMO2015 historical-rcp97	good	good	0.248 (0.190 ... 0.292)	-0.20 (-0.55 ... 0.058)	good
MPI-ESM-LR_MPI-CSC-REMO2009 historical-rcp98	good	good	0.224 (0.175 ... 0.258)	-0.067 (-0.32 ... 0.14)	good
NorESM1-M_GERICS-REMO2015 historical-rcp99	reasonable	good	0.180 (0.141 ... 0.211)	0.023 (-0.39 ... 0.23)	reasonable
NorESM1-M_ICTP-RegCM4-7 historical-rcp100	bad	bad	0.267 (0.203 ... 0.327)	-0.68 (-0.95 ... -0.45)	bad
HighResMIP					
CMCC-CM2-HR4 histSST-present	reasonable	good	0.211 (0.130 ... 0.262)	-0.087 (-0.59 ... 0.24)	reasonable
CMCC-CM2-VHR4 histSST-present	reasonable	good	0.184 (0.132 ... 0.216)	-0.20 (-0.55 ... 0.13)	reasonable
EC-Earth3P-HR histSST-present	good	good	0.203 (0.0972 ... 0.257)	-0.12 (-0.54 ... 0.86)	good
EC-Earth3P histSST-present	good	good	0.187 (0.128 ... 0.231)	0.093 (-0.39 ... 0.62)	good
FGOALS-f3-H histSST-present	good	bad	0.244 (0.174 ... 0.291)	-0.24 (-0.64 ... 0.12)	bad
FGOALS-f3-L histSST-present	reasonable	good	0.210 (0.120 ... 0.266)	-0.12 (-0.55 ... 0.29)	reasonable,1x
HadGEM3-GC31-HM histSST-present	good	good	0.212 (0.144 ... 0.245)	-0.15 (-0.57 ... 0.31)	good
HadGEM3-GC31-LM histSST-present	good	good	0.174 (0.124 ... 0.208)	-0.10 (-0.52 ... 0.12)	good
HadGEM3-GC31-MM histSST-present	good	good	0.191 (0.126 ... 0.236)	-0.26 (-0.75 ... 0.099)	good
HiRAM-SIT-HR histSST-present	good	bad	0.187 (0.134 ... 0.226)	-0.055 (-0.49 ... 0.36)	bad
HiRAM-SIT-LR histSST-present	good	good	0.194 (0.134 ... 0.224)	-0.30 (-0.65 ... 0.36)	good
MPI-ESM1-2-HR histSST-present	reasonable	good	0.181 (0.0892 ... 0.221)	0.017 (-0.32 ... 1.2)	reasonable, 1x
MPI-ESM1-2-XR histSST-present	good	good	0.225 (0.156 ... 0.282)	-0.41 (-0.81 ... -0.22)	good
NICAM16-7S histSST-present	bad	good	0.230 (0.143 ... 0.274)	-0.29 (-0.68 ... 0.36)	bad
NICAM16-8S histSST-present	reasonable	good	0.272 (0.183 ... 0.336)	-0.24 (-0.83 ... 0.14)	reasonable, 2x

4.2 Seasonal (December-March) mean temperature over the IPCC SES region

Table 4.2 Evaluation results of the climate models considered for attribution analysis of DJFM mean temperature over the study region. For each model, the threshold for a 1-in-50-year event is shown, as well as the best estimates of the Sigma parameter, along with 95% confidence intervals. Furthermore evaluation of the seasonal cycle and spatial pattern are shown.

Model / Observations	**Seasonal cycle**	**Spatial pattern**	**Sigma**	**Conclusion**
ERA5			0.352 (0.295 ... 0.404)	
MSWX			0.357 (0.270 ... 0.420)	
CPC			0.467 (0.351 ... 0.548)	
HighResMIP				
EC-Earth3P-HR	good	good	0.417 (0.290 ... 0.510)	good
EC-Earth3P	good	good	0.447 (0.314 ... 0.545)	good
FGOALS-f3-L	good	good	0.603 (0.445 ... 0.697)	reasonable
HadGEM3-GC31-HM	good	good	0.480 (0.357 ... 0.572)	good
HadGEM3-GC31-LM	good	good	0.465 (0.354 ... 0.536)	good
HadGEM3-GC31-MM	good	good	0.405 (0.261 ... 0.499)	good
HiRAM-SIT-HR	good	good	0.462 (0.329 ... 0.540)	good
HiRAM-SIT-LR	good	good	0.438 (0.266 ... 0.591)	good
MPI-ESM1-2-HR	good	good	0.431 (0.291 ... 0.521)	good
MPI-ESM1-2-XR	good	good	0.434 (0.334 ... 0.504)	good
NICAM16-7S	good	good	0.527 (0.373 ... 0.645)	good
NICAM16-8S	good	good	0.505 (0.366 ... 0.585)	good
CORDEX				
CanESM2_r1i1p1_SMHI-RCA4	good	good	0.514 (0.425 ... 0.592)	good
CanESM2_r1i1p1_UCAN-WRF341I	good	good	0.479 (0.409 ... 0.531)	good
CNRM-CM5_r1i1p1_SMHI-RCA4	good	good	0.457 (0.368 ... 0.525)	good

CSIRO-Mk3-6-0_r1i1p1_SMHI-RCA4	good	good	0.517 (0.421 ... 0.595)	good
EC-EARTH_r12i1p1_SMHI-RCA4	good	good	0.607 (0.499 ... 0.701)	reasonable
GFDL-ESM2M_r1i1p1_ICTP-RegCM4-3	good	good	0.587 (0.472 ... 0.685)	reasonable
GFDL-ESM2M_r1i1p1_SMHI-RCA4	good	good	0.464 (0.387 ... 0.524)	good
HadGEM2-ES_r1i1p1_ICTP-RegCM4-7	good	good	0.488 (0.369 ... 0.582)	good
IPSL-CM5A-MR_r1i1p1_SMHI-RCA4	good	good	0.511 (0.435 ... 0.580)	good
MIROC5_r1i1p1_SMHI-RCA4	good	good	0.463 (0.383 ... 0.531)	good
MPI-ESM-LR_r1i1p1_MPI-CSC-REMO2009	good	good	0.586 (0.492 ... 0.660)	reasonable
MPI-ESM-LR_r1i1p1_SMHI-RCA4	good	good	0.597 (0.510 ... 0.672)	reasonable
MPI-ESM-MR_r1i1p1_ICTP-RegCM4-7	good	good	0.535 (0.435 ... 0.606)	good
NorESM1-M_r1i1p1_ICTP-RegCM4-7	good	good	0.693 (0.555 ... 0.803)	bad
NorESM1-M_r1i1p1_SMHI-RCA4	good	good	0.486 (0.402 ... 0.552)	good

5 Multi-method multi-model attribution

This section shows Probability Ratios and change in intensity ΔI for models that passed model evaluation and also includes the values calculated from the fits with observations.

Table 5.1. Event magnitude, probability ratio and change in intensity for 50-year return period for RX7day rainfall over the observational datasets and each model that passed the evaluation tests. (a) from pre-industrial climate to the present and (b) from the present to 2.6℃ above pre-industrial climate

		Current warming level [1.3 ˚C]		Future warming level [2.6 ˚C]	
Model / Observations	**Threshold for return period 10 yr [mm/7day]**	**Probability ratio PR [-]**	**Change in intensity ΔI [mm/7day]**	**Probability ratio PR [-]**	**Change in intensity ΔI [%]**
MSWEP	75.97302	0.37 (0.051 ... 3.0)	-16 (-41 ... 21)		
CPC	88.34234	0.57 (0.013 ... 1.6e+2)	-6.4 (-40 ... 36)		
ERA5	66.25679	0.67 (0.25 ... 1.3)	-11 (-28 ... 8.9)		
Models	**Threshold for return period 50 yr**				
GFDL-ESM2M_r1i1p1_SMHI-RCA4 historical-rcp90	73	2.7 (0.90 ... 11)	19 (-2.1 ... 44)	2.4 (1.2 ... 4.3)	16 (4.1 ... 26)
HadGEM2-ES_r1i1p1_CTP-RegCM4-7 historical-rcp91	1.0e+2	1.0 (0.32 ... 4.8)	0.38 (-15 ... 16)	1.5 (0.79 ... 2.9)	5.8 (-3.7 ... 14)
HadGEM2-ES_r1i1p1_ICTP-RegCM4-3 historical-rcp93	88	0.71 (0.27 ... 4.8)	-5.7 (-23 ... 15)	1.6 (0.98 ... 2.6)	7.2 (-0.30 ... 14)
IPSL-CM5A-MR_r1i1p1_SMHI-RCA4 historical-rcp95	79	2.8 (0.71 ... 34)	12 (-3.8 ... 31)	1.3 (0.67 ... 2.5)	3.1 (-4.1 ... 11)
MIROC5_r1i1p1_SMHI-RCA4 historical-rcp96	63	1.0 (0.35 ... 4.6)	0.54 (-14 ... 19)	1.3 (0.59 ... 2.3)	3.4 (-6.9 ... 12)
MPI-ESM-LR_r1i1p1_GERICS-REMO2015 historical-rcp97	1.0e+2	1.5e+2 (1.2 ... ∞)	34 (1.9 ... 71)	2.7 (1.4 ... 4.7)	15 (5.0 ... 24)
CMCC-CM2-HR4 histSST-present	93	6.8 (1.1 ... 4.1e+2)	23 (0.96 ... 50)		
CMCC-CM2-VH	88	1.0 (0.29 ... 12)	0.033 (-17 ... 21)		

R4 histSST-present					
EC-Earth3P-HR histSST-present	82	2.9 (0.38 ... ∞)	8.1 (-11 ... 31)		
EC-Earth3P histSST-present	87	6.2 (1.1 ... 7.1e+2)	24 (0.85 ... 57)		
FGOALS-f3-L histSST-present	93	12 (0.73 ... ∞)	28 (-4.0 ... 66)		
HadGEM3-GC31-HM histSST-present	87	0.31 (0.12 ... 2.4)	-15 (-35 ... 7.3)		
HadGEM3-GC31-MM histSST-present	1.0e+2	2.1 (0.34 ... 1.1e+3)	6.1 (-12 ... 28)		
HiRAM-SIT-LR histSST-present	87	4.4 (0.54 ... 71)	17 (-7.5 ... 44)		
MPI-ESM1-2-HR histSST-present	86	1.6 (0.28 ... 12)	5.7 (-15 ... 30)		
MPI-ESM1-2-XR histSST-present	81	0.50 (0.17 ... 4.1e+4)	-7.1 (-24 ... 14)		
NICAM16-7S histSST-present	62	0.41 (0.15 ... 6.7)	-12 (-33 ... 20)		
NICAM16-8S histSST-present	74	1.0 (0.30 ... 14)	0.46 (-20 ... 28)		

Table 5.2. Event magnitude, probability ratio and change in intensity for 50-year return period for DJFM mean temperature over the observational datasets and each model that passed the evaluation tests. (a) from pre-industrial climate to the present and (b) from the present to 2.6℃ above pre-industrial climate.

Model / Observations	**Threshold for return period 50 yr** [˚C]	**Current warming level [1.3 ˚C]**		**Future warming level [2.6 ˚C]**	
		Probability ratio PR [-]	**Change in intensity ΔI [˚C]**	**Probability ratio PR [-]**	**Change in intensity ΔI [˚C]**
ERA5	28.70642 ˚C	7.8e+7 (6.0e+5 ... 1.6e+11)	1.4 (1.0 ... 1.7)		
MSWX	28.70078 ˚C	2.3e+10 (5.4e+6 ... 9.7e+18)	1.8 (1.3 ... 2.5)		
CPC	31.15088 ˚C	3.9e+10 (6.9e+6 ... 4.1e+18)	2.5 (1.7 ... 3.3)		
EC-Earth3P-HR	28 ˚C	2.5e+3 (62 ... 6.9e+5)	0.84 (0.50 ... 1.2)		
EC-Earth3P	28 ˚C	20 (1.4 ... 7.4e+2)	0.46 (0.059 ... 0.83)		
HadGEM3-GC31-HM	30 ˚C	7.5e+4 (5.2e+2 ... 3.7e+8)	1.3 (0.87 ... 1.8)		

HadGEM3-GC31-LM	29 ˚C	2.0e+3 (45 ... 3.0e+6)	1.0 (0.56 ... 1.5)		
HadGEM3-GC31-MM	29 ˚C	2.1e+6 (7.3e+3 ... 6.3e+10)	1.3 (0.94 ... 1.8)		
HiRAM-SIT-HR	29 ˚C	5.3e+4 (2.6e+2 ... 1.2e+9)	1.3 (0.80 ... 1.8)		
HiRAM-SIT-LR	29 ˚C	1.5e+3 (49 ... 4.0e+5)	0.98 (0.56 ... 1.5)		
MPI-ESM1-2-HR	28 ˚C	7.7e+4 (1.5e+3 ... 5.9e+7)	1.2 (0.79 ... 1.6)		
MPI-ESM1-2-XR	28 ˚C	1.0e+3 (28 ... 3.0e+5)	0.70 (0.38 ... 1.0)		
NICAM16-7S	32 ˚C	2.0e+2 (7.5 ... 1.3e+4)	0.93 (0.41 ... 1.4)		
CanESM2_r1i1p1_SMHI-RCA4	30 ˚C	2.7e+2 (49 ... 2.0e+3)	0.89 (0.66 ... 1.1)	24 (19 ... 32)	1.0 (0.89 ... 1.2)
CanESM2_r1i1p1_UCAN-WRF341I	30 ˚C	2.1e+2 (34 ... 2.8e+3)	0.80 (0.56 ... 1.0)	24 (18 ... 32)	0.96 (0.84 ... 1.1)
CNRM-CM5_r1i1p1_SMHI-RCA4	31 ˚C	1.6e+4 (4.3e+2 ... 5.2e+6)	1.2 (0.86 ... 1.6)	37 (27 ... 46)	1.4 (1.1 ... 1.6)
CSIRO-Mk3-6-0_r1i1p1_SMHI-RCA4	30 ˚C	2.1e+4 (2.1e+2 ... 1.9e+7)	1.4 (0.84 ... 1.9)	32 (21 ... 42)	1.4 (1.1 ... 1.6)
GFDL-ESM2M_r1i1p1_SMHI-RCA4	30 ˚C	2.0e+3 (64 ... 8.3e+5)	1.0 (0.62 ... 1.5)	29 (20 ... 38)	1.1 (0.87 ... 1.3)
HadGEM2-ES_r1i1p1_ICTP-RegCM4-7	32 ˚C	2.7e+2 (16 ... 2.9e+4)	0.85 (0.50 ... 1.2)	30 (21 ... 41)	1.2 (1.0 ... 1.4)
IPSL-CM5A-MR_r1i1p1_SMHI-RCA4	31 ˚C	3.6e+4 (1.6e+3 ... 4.1e+6)	1.4 (1.1 ... 1.7)	42 (35 ... 47)	1.5 (1.3 ... 1.7)
MIROC5_r1i1p1_SMHI-RCA4	30 ˚C	1.1e+3 (40 ... 8.2e+4)	0.96 (0.58 ... 1.3)	33 (25 ... 43)	1.3 (1.0 ... 1.5)
MPI-ESM-MR_r1i1p1_ICTP-RegCM4-7	33 ˚C	3.3e+2 (13 ... 6.8e+4)	0.96 (0.47 ... 1.5)	30 (21 ... 40)	1.2 (0.99 ... 1.4)
NorESM1-M_r1i1p1_SMHI-RCA4	29 ˚C	3.4e+3 (84 ... 8.3e+5)	1.1 (0.71 ... 1.5)	27 (19 ... 38)	1.1 (0.91 ... 1.4)

6 Hazard synthesis

For the event definitions described above we evaluate the influence of anthropogenic climate change on the events- RX7day and the DJFM mean of TMax, area-averaged over the respective study regions (see figure 1.2) by calculating the probability ratio as well as the change in intensity using observations from weather stations, reanalysis data and climate models. Models which do not pass the evaluation described above are excluded from the analysis. The aim is to synthesise results from models that pass the evaluation along with the observations-based products, to give an overarching attribution statement.

Figures 6.1 and 6.3 show the changes in probability and intensity for the observation-based products (blue) and models (red). Before combining them into a synthesised assessment, first, a representation error is added (in quadrature) to the observation-based products, to account for the difference between observations-based datasets that cannot be explained by natural variability. This is shown in these figures as white boxes around the light blue bars. The dark blue bar shows the average over the observation-based products. Next, a term to account for intermodel spread is added (in quadrature) to the natural variability of the models. This is shown in the figures as white boxes around the light red bars. The dark red bar shows the model average, consisting of a weighted mean using the (uncorrelated) uncertainties due to natural variability. A more detailed description as well as the underlying equations can be found in Otto et al., (2024).

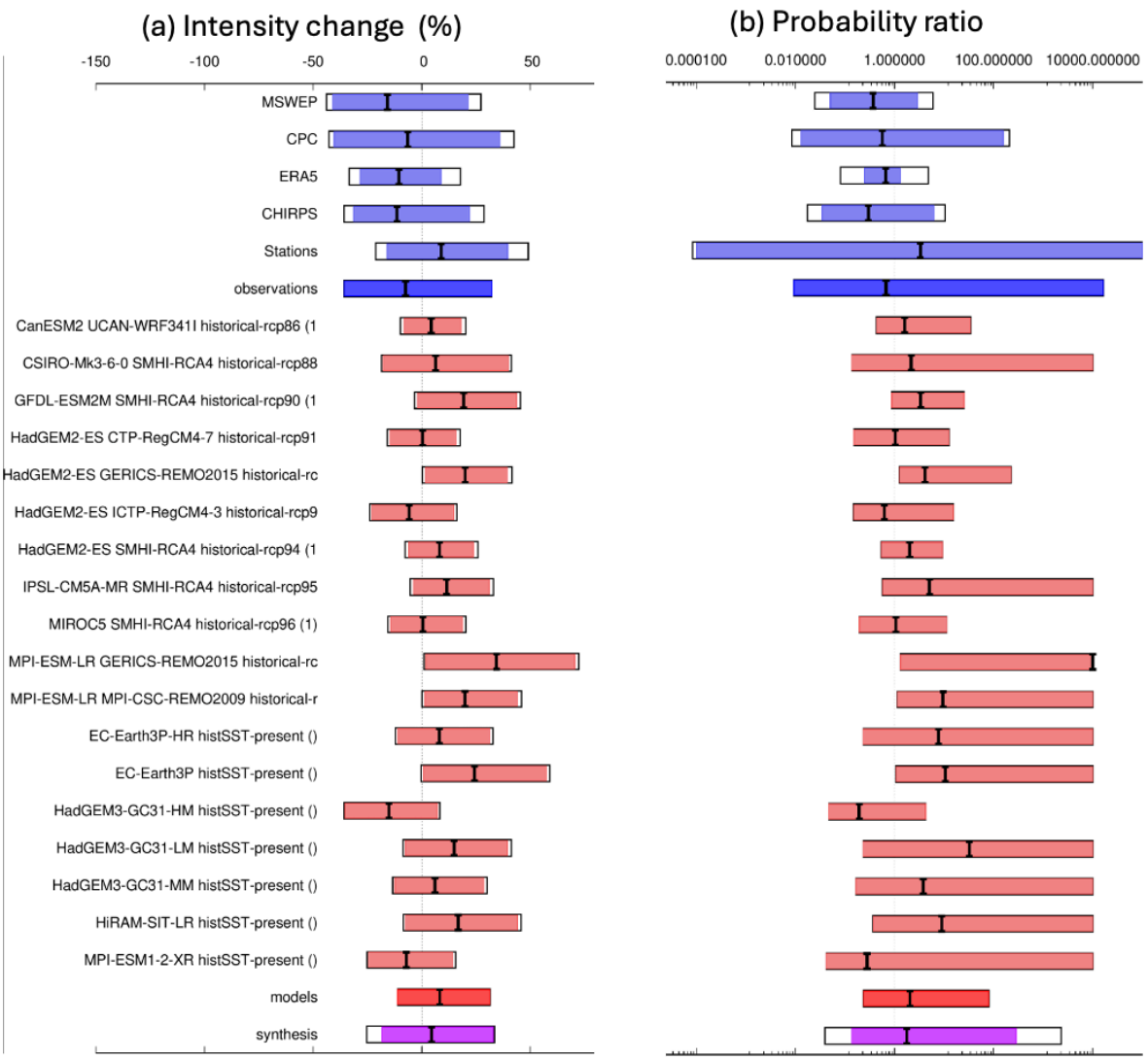

Figure 6.1: Synthesis of (a) intensity change and (b) probability ratios when comparing RX7day over the study region with a 1.3℃ cooler climate.

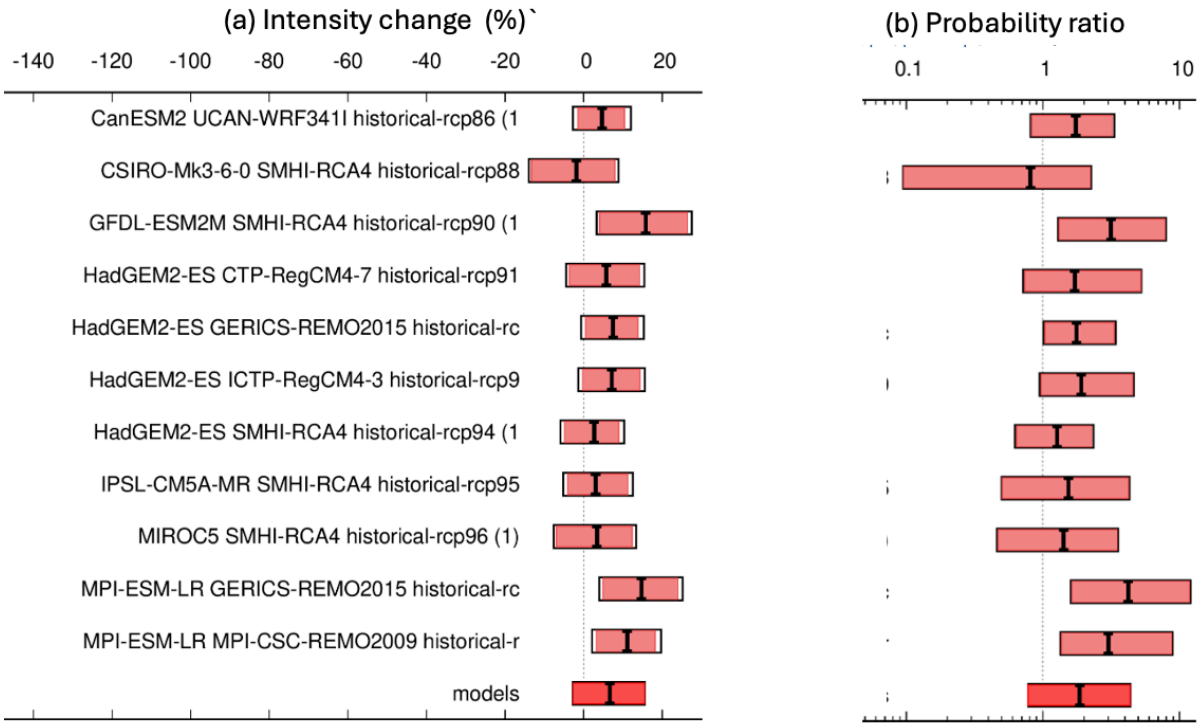

Figure 6.2: Synthesis of (a) intensity change and (b) probability ratios when comparing RX7day over the study region with a 1.3℃ warmer climate.

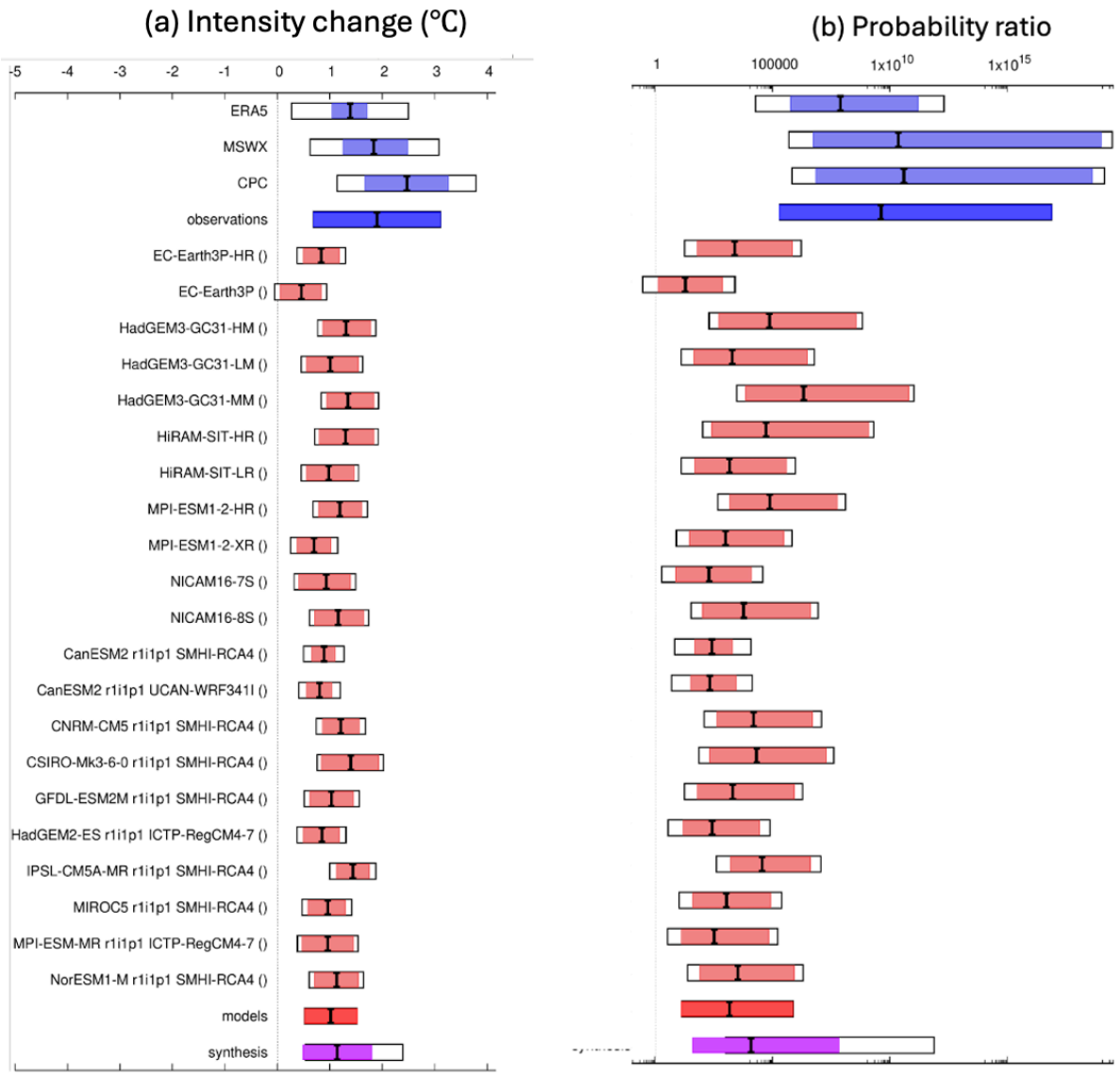

Figure 6.3: Synthesis of (a) intensity change and (b) probability ratios when comparing average TMax during DJFM over the study region with a 1.3℃ cooler climate.

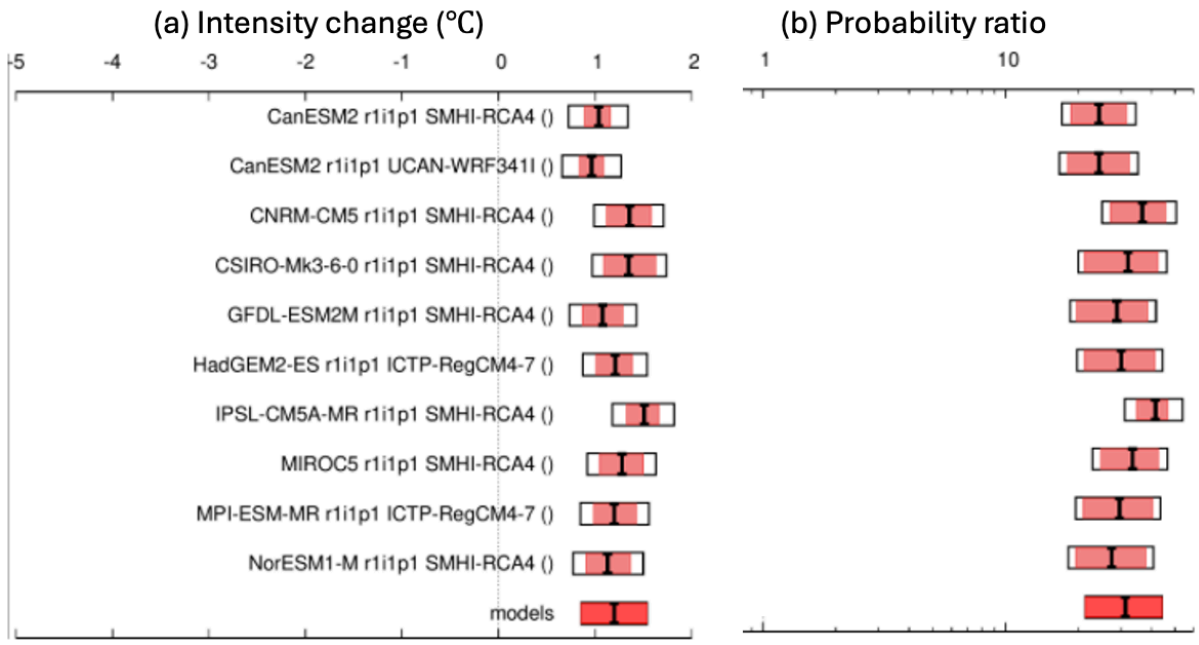

Figure 6.4: Synthesis of (a) intensity change and (b) probability ratios when comparing average TMax during DJFM over the study region with a 1.3℃ warmer climate.

Observation-based products and models are combined into a single result in two ways. Firstly, we neglect common model uncertainties beyond the intermodel spread that is depicted by the model average, and compute the weighted average of models (dark red bar) and observations (dark blue bar): this is indicated by the magenta bar. As, due to common model uncertainties, model uncertainty can be larger than the intermodel spread, secondly, we also show the more conservative estimate of an unweighted, direct average of observations (dark blue bar) and models (dark red bar) contributing 50% each, indicated by the white box around the magenta bar in the synthesis figures. The numerical results are also shown in table 6.1 and the synthesised PR and intensity changes for the weighted synthesis averages along with the uncertainty bounds for both events.

For the rainfall event, the observations from weather stations suggest an overall increase in the intensity and likelihood of extreme rainfall events such as the 2025 event in today's climate which is 1.3°C warmer as compared to the pre-industrial levels, albeit with large uncertainties. This is also the case for each individual weather station, as discussed in section 3. In contrast, the reanalysis products all show a decreasing trend. The majority of the climate models show an increase comparable to the station data.

Figure 6.2 shows the same calculations as in figure 6.1, but comparing the event in climate models as it occurred today, in the 2025-climate, to a 1.3℃ warmer climate. Again, the majority of the models show an increase in the likelihood and intensity of the RX7-day event with future warming of the same magnitude as projected up until now.

The model data as well as the station data show an increase in heavy rainfall that is of the same order of magnitude as would be expected based on the Clausius-Clapeyron relationship in a warming world. Thus, taking these three lines of evidence, the physical expectations, the station data and the models we conclude that human-induced climate change likely did increase the likelihood and intensity of the rainfall event. However, as we cannot reconcile the station data and the reanalysis data, uncertainty in this result is high and we cannot make a conclusive statement. Given that many large scale assessments and adaptation advice is built on gridded reanalysis data, it is important to investigate and understand the differences between station data and gridded reanalysis data in this region.

In contrast, there is a very strong signal from human-induced climate change in the heat event. As shown in figure 6.3 for the past and figure 6.4 for the future, all reanalysis products and models show a strong increase in the likelihood and intensity of the event. The intensity change is about 2℃ in the reanalysis and about 1℃ in the models while the probability ratio is several orders of magnitude, even for the lower bound in the reanalysis and at least in the order of 10 in the model synthesis (dark red bar). We thus conclude that the event that is still comparably rare today, with a return period of 50 to 100 years (see section 3) would have been extremely unlikely to occur without human induced climate change. In a climate of 2.6℃ above the pre-industrial GMST such an event would however be a common occurrence, given the models show an probability ratio for the future of about 30, which, given the large and common (see van Oldenborgh et al., 2022, Schumacher et al., 2022) discrepancy between reanalysis and models is likely a conservative estimate.

When calculating the changes in likelihood and intensity for the hot and humid period preceding the rainfall event we find very similar results for the role of human-induced climate change (see section 3), despite using a different variable and time period.

Data	**GMST: RX7day (Orange alert region)**			**GMST: TMax_DJFM (SES region)**	
		Probability ratio (95% CI)	**Intensity change (%) (95% CI)**	**Probability ratio (95% CI)**	**Intensity change (%) (95% CI)**
Observations	**Past-Present**	0.674 (0.00928… 16200)	-7.39 (-35.7 … 32.30	**0.416E+10 (0.198E+06… 0.770E+17)**	**1.90 (0.695 … 3.12)**
Models		2.07 (0.239 … 79.9)	8.37 (-11.1 … 31.5)	**0.145E+04 (13.6… 0.765E+06)**	**1.02 (0.520 … 1.52)**
Synthesis		1.77 (0.136 … 283)	4.56 (-18.3 … 33.0)	**0.123E+05 (39.7… 0.668E+08)**	**1.15 (0.496 … 1.80)**
Models only	**Present-Future**	1.86 (0.781 …4.37)	6.66 (-2.69 …15.6)	**31.2 (21.3… 44.2)**	**1.20 (0.861 … 1.54)**

Table 6.1: Summary of results for annual (Jul-June) rx7day and DJFM average TMax, area averaged over the study region, presented in Fig1.2(a-b). Changes due to GMST include past-present changes and present-future changes. Increases (decreases) in probability and intensity are highlighted in blue (orange), and statistically significant changes are highlighted in bold.

7 Vulnerability & Exposure

Buenos Aires, Argentina's most populous and economically significant province, spans diverse geographic and climatic conditions, from the dense urban landscape of Buenos Aires to the coastal and low-lying river basins such as Bahía Blanca. This analysis covers the broader area encompassing both Buenos Aires Province and the Autonomous City of Buenos Aires (CABA), given their interconnected geographies and infrastructure, and shared exposure to the studied events. Throughout this analysis, the term "the area" refers to this combined region unless specified otherwise.

The recent heatwave over March 5-7, followed by catastrophic flooding on March 7, highlights the increasing risks posed by meteorological events in this area, particularly for communities in vulnerable situations. CABA, the capital city, experienced a heatwave with temperatures exceeding 35C. The urban heat island effect exacerbated heat stress, particularly in informal settlements where residents have limited access to cooling infrastructure and reliable water supply. Vulnerable groups, including older adults, children, and low-income populations, faced heightened risks due to pre-existing health conditions, poor housing conditions, and limited access to air conditioning (Atlantic Council, n.d.; Fontan & Rusticucci, 2021; Kristoff et al., 2020).

In Bahía Blanca, a major port city in the province with over 330,000 residents, extreme rainfall of 290mm in only 12h (SMN, 2025) triggered severe flooding. Situated in the lower basin of the Napostá stream, the city is highly vulnerable to flash floods. The overflowing of the Napostá stream and the Maldonado canal left large parts of the area submerged, with floodwaters exceeding two meters in some neighborhoods (Doermann, 2025; Gardel & Marina, 2025). Damage to infrastructure was extensive, forcing evacuations, and disrupting essential services (Gobierno de la Provincia de Buenos Aires, 2025; Phys, 2025). The scale of the event far surpassed historical precedents of 151mm in 1975 (SMN, 2025). While Bahía Blanca has experienced severe storms in the past, including one in December 2023 which caused the deaths of 13 people and the displacement of another 700 (IFRC, 2023), this event was defined by extreme rainfall rather than wind damage (Gardel & Marina, 2025).

The co-occurring events of this study highlight the broader challenges of managing increasingly frequent and intense hazards in the area, where vulnerabilities are shaped by urban planning, infrastructure inadequacies, and social inequalities. The following sections will examine the risks of co-occurring extreme heat and flooding, the influence of urban planning and informality in shaping exposure, how disparities in water, electricity, and health systems influence resilience, and the role of disaster risk management in addressing such crises.

7.1 Urban Planning and Informality

The co-occurring heatwave and flood events in Argentina significantly impacted urban areas and large parts of the population as 92% reside in urban areas (World Bank, 2023). Vulnerabilities stem from urban planning and informality, increasing the risk of heat and flood impacts.

In Bahía Blanca, the growth of the city outpaced the interventions to provide the most unprotected areas with adequate infrastructure. This has contributed to problems such as waterlogging or erosion on unpaved streets. Especially in the peripheral neighbourhoods, a lack of levelling of streets and the loss of efficiency of the drainage network cause flood impacts (Zapperi, 2012). Additionally,

development in higher areas accelerated runoff due to impervious surfaces and landfilling (Burdman, 2025). Built up areas increased between 1985-2020 significantly faster than green spaces that could offset some flood (and heat) impacts. Also, green areas are fragmented and lower in flood prone areas and informal settlements (Duval & Ramos, 2023). Green spaces alone cannot offset current flood impacts, however, even 30mm of rain in 24 hours caused frequent floods, evacuations, and disruptions, particularly in southern areas in the past (see below) (Lambrecht & Zapperi, 2024).

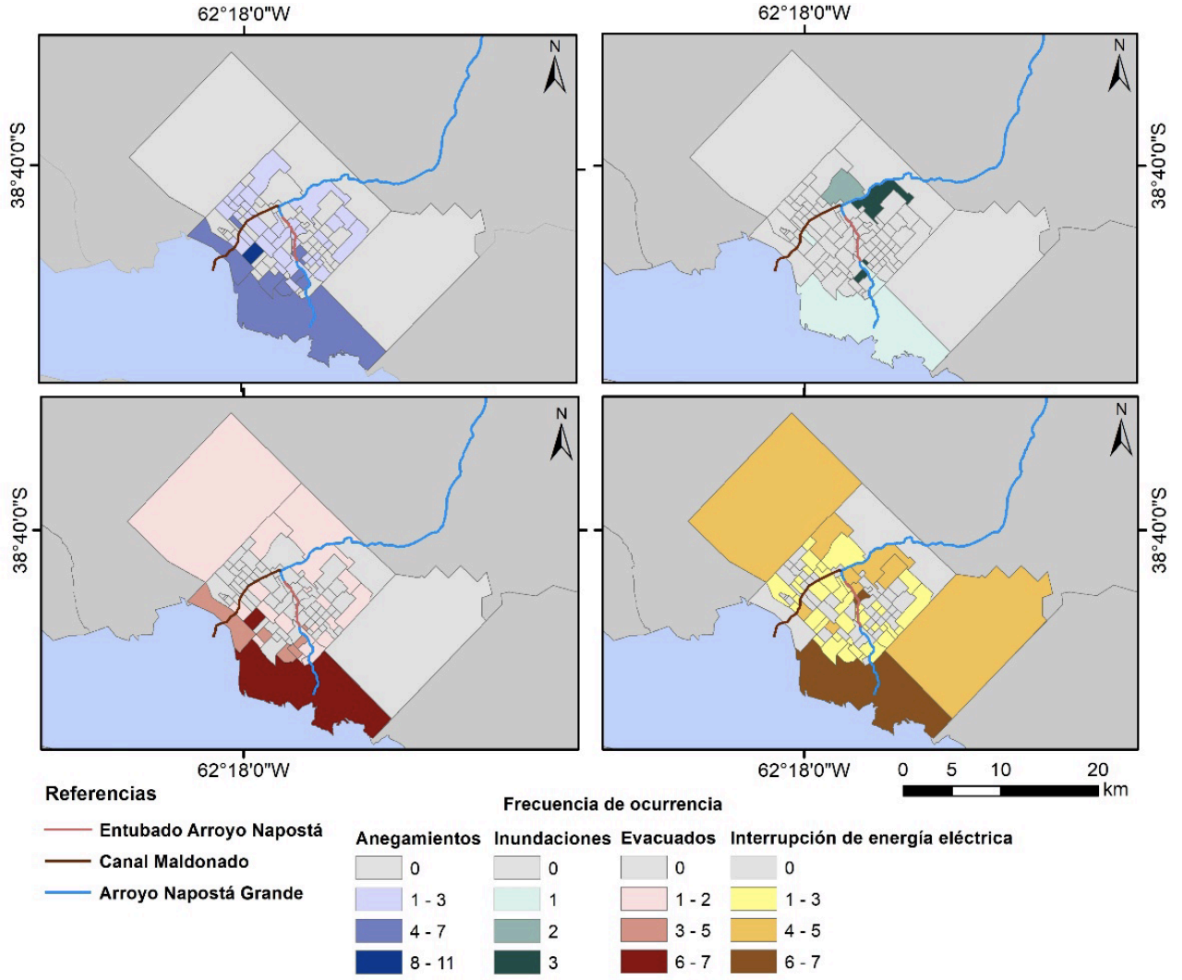

Figure 7.1: *Figure shows Bahía Blanca's areas affected by waterlogging (blue), flooding (green), evacuations (red), and power shortages (yellow) based on newspaper articles (Lambrecht & Zapperi, 2024).*

Green spaces and built up areas also shape heat vulnerabilities, by contributing or mitigating the Urban Heat Island (UHI). The UHI effects in Argentina are not straightforward and not well explored (Palme et al., 2020). Comparing 55 cities, only 60% exhibit an UHI effect during the day, while 40% are urban cold islands. The majority of cities with UHI are located in the heat stricken north, and notably all cities show UHI at night (Casadei et al., 2021). For example, Camilloni & Barrucand (2012) concluded that UHI in Buenos Aires are more pronounced in the morning hours, but in afternoons a cooling effect occurs, which might occur due to receding near clear-sky conditions, declining calm frequencies and an increasing wind speed. In the affected city of Córdoba, several micro UHI have been identified that coincide with high social vulnerabilities due to age, overcrowded households, lack of access to public sewage systems and lower educational level. UHI are in areas with medium to high population density and mid-rise buildings in lower income neighborhoods. UHI

in high income areas are likely due to a high percentage of elderly populations and privatised sewage systems (Faustinelli et al., 2024). Also Bahía Blanca has seen an increased UHI effect due to rapid population growth and increased building density between 1985 and 2014 (Ferrelli et al., 2016). Flores-Larsen & Filippín (2021) highlight that in low income neighborhoods, ambient temperatures exceed 32-40°C in the majority of households, leaving especially elderly, people with disabilities, and children, chronically exposed to dangerous temperatures in their homes.

While many coped with the heat by seeking cooling in parks, or malls (Global Times, 2025), the accessibility is lower among vulnerable populations trapped at home, and within informal settlements. Around 16% of the urban population resides in informal settlements (World Bank, 2023). The largest accumulations are seen in Buenos Aires with nearly 500,000 families, however other affected cities such as Bahía Blanca or Córdoba grapple with informality too (see below) (Vera et al., 2022). Vulnerabilities manifest through low access to formal running water (6.2%), sewage systems (1.2%) and electricity (29.3%), making these neighbourhoods vulnerable to floods and heat waves alike (Vera et al., 2022).

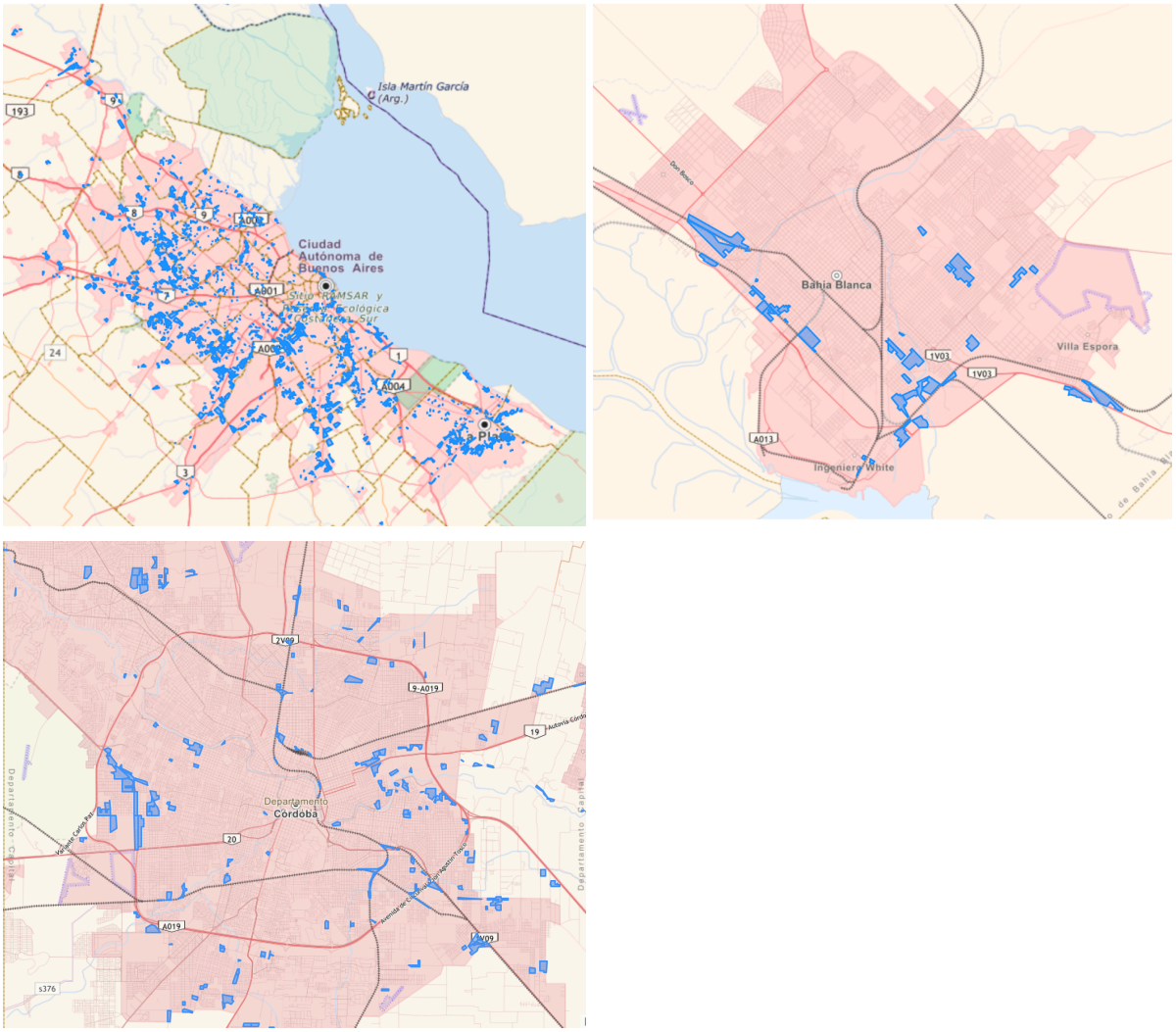

Figure 7.2: *Registered informal settlements (areas in Blue) in Buenos Aires, Bahía Blanca, and Córdoba (left to right) (Registro Nacional de Barrios Populares 2022).*

Informality in the economy adds another layer of vulnerability and is especially concentrated among the urban poor in informal settlements as they face barriers and discrimination entering the formal job markets (Zanoni, 2022). Almost 50% of the urban population is employed in the informal economy, and particularly highly concentrated among self-employed individuals (80% of all self-employed) (Maurizio & Monsalvo, 2021). Consequently, a large proportion of the urban livelihoods are sensitive to climate shocks, for example due to employment disruption and exposure to heat. There is a general lack of studies on occupational heat stress in South America, including Argentina (De Sario, 2023), but it is estimated that most productivity loss due to extreme heat is seen in the construction work, followed by service industry and manufacturing, which is often subject to informal employment (Lancet Countdown, 2024).

In Buenos Aires, the informal settlement of Villa 20 exemplifies how participatory upgrades can integrate climate justice and adaptation. Supported by Transformative Urban Coalitions, the initiative combines decarbonization with efforts to reduce UHI, improve drainage, and enhance local resilience through nature-based solutions (NbS) (UN Habitat, 2024; Kibii et al., 2025). Implemented NbS include permeable pavements, vertical gardens, rain gardens, and tree planting using native species. Community workshops co-designed these measures, which also helped raise awareness and foster ownership. These interventions not only created microclimates and improved stormwater management but also created shaded communal areas and boosted social cohesion (Kibii et al., 2025).

Similarly, the Rodrigo Bueno upgrading initiative has formalised housing, introduced drainage and sewage infrastructure, and preserved green spaces through a collaborative planning process with residents (C40, 2022). The project integrates climate resilience and social inclusion, demonstrating that even dense informal settlements can be transformed into safer, more sustainable communities when approached through a rights-based and participatory process.

Beyond physical exposure, the capacity of critical infrastructure and public services to absorb shocks plays a decisive role in determining disaster outcomes. The extent to which water, electricity, and health systems withstood these events shed light on both immediate challenges and long-term resilience needs.

7.2 Water, Electricity, and Health Systems

Buenos Aires Province and the Autonomous City of Buenos Aires have implemented several measures to enhance resilience to heatwaves and floods, though challenges remain due to increasing climate extremes. Efforts to improve water, electricity, and health systems have shown progress over the past decade, particularly in terms of infrastructure development, adaptation planning, and cross-sectoral planning.

In the water sector, authorities have prioritized both structural and Nature based Solutions to reduce urban flood risk and support long-term adaptation. The Hydraulic Masterplan, initiated in 2006 and still ongoing, has guided the upgrading of major drainage basins such as the Maldonado, Vega, and Cildánez, with large-scale work designed to channel stormwater to the Río de la Plata (World Bank, 2021). These traditional grey infrastructure investments have been increasingly complemented by green solutions, including urban ecological corridors, infiltration basins, and permeable surfaces

aimed at slowing runoff and increasing groundwater recharge. However, during the March 2025 flood in Bahía Blanca, water and sewage systems were compromised, with pipe damage and strees collapses leading to reliance on tanker trucks for emergency water distribution (Government Province of Buenos Aires, 2025). Severe damage was also reported to the embankments and bridges of the Maldonado Canal, one of the key components of the city's hydraulic system. Available initial information suggests that this infrastructure was designed for standard storm events, of up to 30-50 mm per hour - well below the 290 mm recorded in just 12 hours (Gardel & Marina, 2025). This discrepancy raises important questions about current design standards and the need to adapt infrastructure for changing climate conditions. A comprehensive damage and needs assessments, including forensic engineering analysis, is recommended to evaluate performance and inform future upgrades. As concerns grow over potential building collapses, engineers have already begun actively assessing the stability of foundations throughout the city (Yadav, 2025).

In the energy sector, the government has expanded access to renewable and efficient technologies in both rural and urban areas. The Clean Energy for Vulnerable Households Initiative, which focuses on solar power and energy-efficient appliances, has reached over 200,000 people in off-grid or underserved communities (World Bank, 2023). Nonetheless, urban electricity systems remain exposed during high-demand periods. During the March 2025 heatwave, CABA experienced widespread power outages affecting around two million residents, highlighting the need for improved resilience in electricity distribution, particularly in neighborhoods with precarious or informal connections. The March flood event also tested Bahía Blanca's power grid resilience. Although electricity supply was temporarily disrupted due to damage to substation, power was restored to 99% of affected areas within days (Government Province of Buenos Aires, 2025).

Buenos Aires continues to scale up energy efficiency initiatives, including the replacement of public lighting with LED technology (now covering over 60% of the city) and the retrofitting of municipal buildings. Plans for decentralized energy generation are supported by resource mapping initiatives, such as the development of solar and wind potential assessments (Gobierno de la Ciudad de Buenos Aires, 2020). Further, urban greening efforts, coordinated under the Urban Tree Master Plan, contribute to passive cooling and reduced energy demand for air conditioning. These combined efforts are intended to reduce peak load stress, particularly during heatwaves, and improve equity in access to essential energy services.

In the health sector, the impacts of extreme heat have been well documented. Research has shown a marked increase in mortality associated with heatwaves, particularly in cases involving hypertensive and cardiovascular disease. During the 2013 event, over 480 excess deaths were recorded in Buenos Aires (Fontan & Rusticucci, 2021). The city has since implemented a suite of public health interventions designed to reduce temperature-related risks, including seasonal awareness campaigns and enhanced hospital readiness protocols.

Despite these measures, disparities in health vulnerability remain. Southern communes with higher concentrations of informal settlements rely more heavily on public services, face higher burdens of chronic illness, and often experience compounded exposures due to poor housing quality and limited access to green spaces (Fontan & Rusicucci, 2021; Kibii et al., 2025). In response, city authorities have begun integrating health indicators into climate risk mapping an expanded training for municipal health staff to better prepare for future climate-health risks. Disease surveillance systems are also

being enhanced to better monitor and respond to climate-sensitive conditions such as dengue, leptospirosis, and diarrheal illnesses, which tend to spike during extreme rainfall or heat events.

In parallel, local upgrading initiatives such as those in Villa 20 demonstrate the value of integrated investments in housing, green infrastructure, lighting, and drainage. Co-developed through participatory processes, these projects contribute not only to physical risk reduction but also to improved access to essential services and community wellbeing (Kibii et al., 2025).

In the March floods, health services were affected in a number of ways. In Bahía Blanca, evacuations included patients and staff from the José Penna hospital, which houses critical care units including a neonatal ward (Argentine Red Cross, 2025). Damage to transport infrastructure and disrupted access routes added complexity to the emergency health response. These challenges highlight the importance of ensuring continuity of care and functional health infrastructure during weather-related disasters. Indeed, the disruptions to essential services highlight the importance of proactive disaster risk management strategies that address early warning, anticipatory action, response and adaptation.

7.3 Disaster Risk Management

The Buenos Aires province, along with CABA, face increasing disaster risk due to the intersecting trends of climate change, rapid urbanization, and demographic shifts, particularly an aging population. Rising temperatures and intensified rainfall events pose challenges for disaster risk management systems, notably in urban centres where rapid expansion has placed pressure on existing infrastructure. Informal settlements, which house a significant portion of the population, often experience greater exposure to heat and flooding due to limited access to drainage, cooling infrastructure, and emergency services (Kibii et al., 2025). The recent extreme heat in Buenos Aires on March 5-7, followed by severe flooding in Bahía Blanca on March 7, highlight the complexity of managing co-occurring hazards and the importance of coordinated preparedness and response efforts. This sequence of events also underscores the need to move beyond single-hazard approaches and toward risk governance strategies that account for compound and cascading risks including multi-hazard early warning systems.

Between March 5 and 7, the National Meteorological Service (SMN) issued heat alerts across multiple provinces in response to forecasted high temperatures. Buenos Aires and its suburbs were placed under a yellow alert, signaling potential health risks, particularly for vulnerable groups such as older adults and those with pre-existing conditions (Xinhua, 2025). Later, SMN issued a yellow alert for heavy rainfall over Bahía Blanca 28 hours before the flood, which was upgraded to orange on March 6 and then red on March 7 as conditions intensified. This progression followed established protocols (Saucedo et al., 2023), and authorities took precautionary measures, including suspending outdoor activities, ordering school closures, and issuing a precautionary power outage throughout the region. A total of 1,236 displaced individuals were accommodated in 13 evacuation centers established to provide shelter and assistance (Yadav, 2025). Further, the airport and port were closed, and public transportation services were suspended (Bianco, 2025). More than 2,500 people were evacuated overall, including staff and patients from the José Penna hospital which includes critical care units (Argentine Red Cross, 2025).

Emergency response efforts were mobilized, with evacuation centers opened and assistance programmes activated. The extreme rainfall in Bahía Blanca led to road closures and bridge damage, leaving parts of the city cut off while creating logistical challenges for response teams (Government Province of Buenos Aires, 2025; BBC, 2025). Government subsidies were allocated to support 33,000 low- and lower-middle-income families affected by the disaster, with a total investment of 26 million pesos ($23,390 USD). Additionally, an urban infrastructure repair fund was established, amounting to 75 million pesos ($70,170 USD). Overall, public investment in response to the disaster exceeded 273 billion pesos (255 million USD) (Government Province of Buenos Aires, 2025).

As extreme weather events become more frequent, continued investment in early warning systems and anticipatory action, risk-informed urban planning, and integrated preparedness built on multi-hazard assessments will remain important priorities in strengthening resilience. Nature based Solutions (NbS) such as rain gardens, oxygen corners, wetlands, and urban tree cover can reduce both heat and flood risks while offering social and environmental co-benefits (Singh & Pereira Marghidan, 2025; Kumar et al., 2024; Kozak et al., 2020). Further, projects like in the Rodrigo Bueno neighborhood and Villa 20 in Buenos Aires can reduce informality through partnership and shared decision-making with the residents of informal settlements, yielding results including a formalisation of the area with a new street system, and official registration of business and home addresses which allow for formal employment and improved access of emergency services (Climate Adaptation Platform, 2024; UN Habitat, 2024; Kibii et al., 2025; C40, 2022).

7.4 Compounding Risks and Multi-Hazard Adaptation

In Northern Argentina, including the Buenos Aires province and CABA, extreme heat and heavy rainfall events have intensified and occur more frequently in recent decades, including simultaneous or sequential extremes such as heat-heavy rainfall or hot-dry events (Tencer et al., 2016; Bevacqua et al., 2022). This heightens the risk of compounding hydrometeorological hazards. Regional studies report rising trends in both heat and precipitation extremes, with events such as the 2013 La Plata flood, November-December 2022 heatwave, and December 2023 Bahía Blanca storm underscoring these growing risks (Etulain & López, 2017; Lambrecht et al., 2024; Penalba & Robledo, 2010; Cerón et al., 2021; Collazo et al., 2024). Human-induced climate change has been a key driver of these trends (Rivera et al., 2023; Kew et al., 2023; IPCC, 2023). From the second half of February 2025, the extreme heat over northern Argentina, southern Brazil and much of Paraguay and Uruguay led to temperatures above 40°C. This extended period of hot weather and high atmospheric humidity led to extreme rainfall conditions over Bahía Blanca in the first week of March. This study's attribution analysis finds that the 2024/25 heat event would have been virtually impossible in a climate 1.3℃ cooler, but may become common at 2.6℃. Models also suggest an increased likelihood of intense rainfall, suggesting growing risk of compound flood-heat extremes.

Other hazards are also intensifying. The 2022/23 drought, Argentina's worst in 60 years, was partly driven by natural variation but also exacerbated by record-breaking temperatures that worsened evaporation (Arias et al, 2023). Compound hot-dry events, increasingly common in the Pampas, are driven by warming, precipitation variability, and La Nina conditions (Lopez-Ramirez et al., 2024; Collazo et al., 2023). In southeastern South America, including northeastern Argentina, such events are increasingly linked to wildfires, reduced water availability, and decreased crop yields (Pierrestegui

et al., 2025).

CABA's aging population, unequal urban development, and high population density increase both exposure and vulnerability to hazards (Gobierno de la Ciudad de Buenos Aires, 2020). The city's Climate Action Plan (CAP 2050) highlights that nearly 20% of residents will be over 65 by 2040 - an age group particularly vulnerable to heat-related health risks and disruptions in healthcare services during extreme events. Meanwhile, informal settlements, often located in low-lying or heat-exposed areas, frequently lack adequate drainage systems, access to cooling, and quality healthcare, making residents disproportionately susceptible to both floods and heatwaves. The high population density of CABA further amplifies these challenges by intensifying pressure on critical infrastructure, such as water, energy, transport, and emergency response systems. These socio-spatial vulnerabilities not only increase the direct impacts of extreme events but also create pathways for cascading failures, where one disruption (e.g. flooding) may trigger or intensify others (e.g. power outages, heat-related illness).

CAP 2050 argues that rising heatwaves, floods, and storms increasingly co-occur and disproportionately affect the most vulnerable, demanding an integrated nature-based adaptation to reduce cascading risks. In response, the city has implemented a range of structural and social measures. These include major hydraulic infrastructure works, such as the expansion of stormwater networks and underground tunnels in key watersheds, combined with NbS such as green spaces and tree planting to reduce urban heat and improve water retention. Early warning systems and real-time storm alerts are paired with emergency protocols and community training. Health infrastructure has been expanded, ensuring that no resident lives more than 15 minutes from a health centre. Informal settlements are being integrated through housing upgrades, expanded access to basic services, and improved mobility. Measures also encompass green school programs and awareness-raising actions. Through jurisdictional coordination, CAP 2050 also addresses risks that transcend city boundaries, such as watershed flooding and regional transport systems.

Some 630km south of CABA, Bahía Blanca has also taken steps to improve its adaptation to hydrometeorological hazards. Early warning capacities have improved with over 11 monitoring stations along the Bahía Blanca-Viedma corridor, providing real-time rainfall and soil moisture data (AF-TERG, 2024; IDB Adaptation Fund, 2024). Further, climate advisories are provided to farmers to support agricultural adaptation, including anticipatory measures for climate variations, and training programs are offered to build capacity for interpreting and managing climate data (AF-TERG, 2024).

However, while admittedly very extreme, the March 2025 flooding in Bahía Blanca exposed critical stress points in existing adaptation measures. The intensity of the rainfall appears to have exceeded realistic design thresholds, overwhelming drainage capacity in several parts of the city. At the same time, limitations in updated floodplain mapping have left parts of the city without accurate risk information. As weather and climate extremes grow more complex and interconnected, strengthening cross-sectoral planning remains an important opportunity for building resilience. The same is true for CABA. While CAP 2050 offers a strong basis for adaptation, recent heatwave-induced blackouts suggest residual vulnerability of the energy grid and a need to further strengthen continuity across critical systems to ensure coordinated resilience between energy, health, and emergency infrastructure.

In general, compound flood and heat events demand adaptation strategies that account for cross-hazard interactions (such as flood-induced power outages during heatwaves) and prioritize

interventions with co-benefits (such as flood-resilient cooling centres, NbS like afforestation and rain gardens, and multi-hazard early warning systems) (Singh & Pereira Marghidan, 2025). Planning processes should anticipate compounding and cascading dynamics to avoid maladaptive trade-offs (such as building hard flood protection infrastructure which risks worsening urban heat) and ensure continuity across critical infrastructure systems. However, risks and needs are highly contextual. Robust after-action reviews, impact assessments, and cross-sector evaluations will be essential to identify the key risk drivers, clarify causal pathways, and inform the design of locally grounded, climate-smart recovery and adaptation measures to reduce risk and enhance systemic resilience in the affected areas.

V&E Conclusions

This analysis highlights the growing complexity of vulnerability and exposure in Buenos Aires Province and CABA amid intensifying weather extremes, particularly with increasing risk from compounding events. The March 2025 flood in Bahía Blanca caused unprecedented damage due to record-breaking rainfall, with infrastructure limitations and floodplain planning gaps likely contributing to the extent of the disruption. In CABA, the heatwave led to electricity blackouts driven by heightened energy demand. While no evidence of compounding impacts has been identified between the two events, climate change is increasing the likelihood of simultaneous and cascading hazards, including flood-heat extremes and other hydrometeorological and social shocks. Efforts to strengthen continuity across critical infrastructure systems and invest in solutions with co-benefits will be vital to address these risks. Forward-looking, context-specific planning grounded in inclusive governance and local risk knowledge remains essential to reduce exposure, build resilience, and support equitable adaptation across affected communities.

Data availability

All time series used in the attribution analysis are available via the Climate Explorer.

References

All references are given as hyperlinks in the text.

Appendix

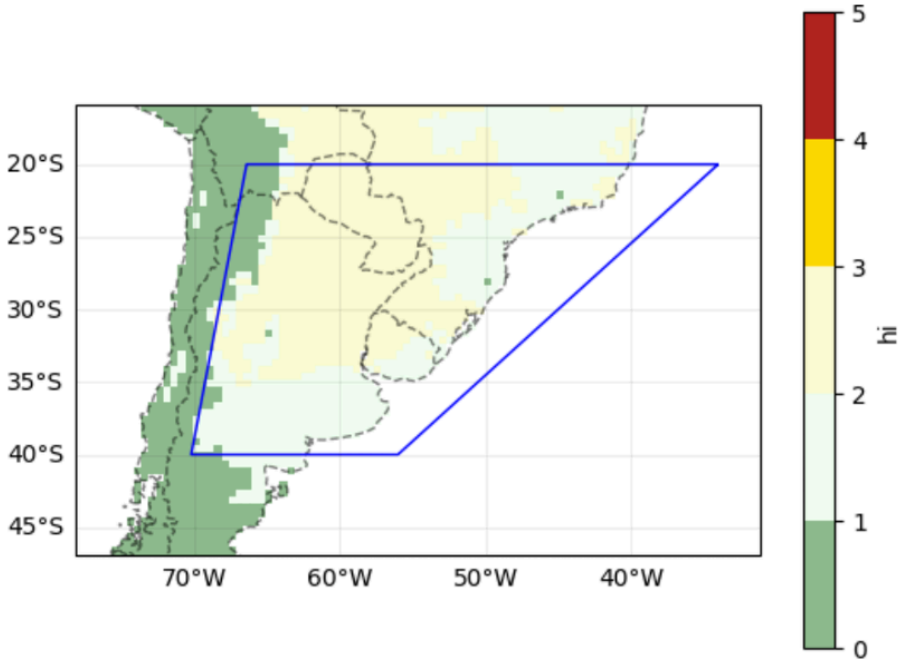

Figure A1: Classification map for heat impacts based on HI, for the 21-day average daily HI for the period 15 February - 7 March 2025.

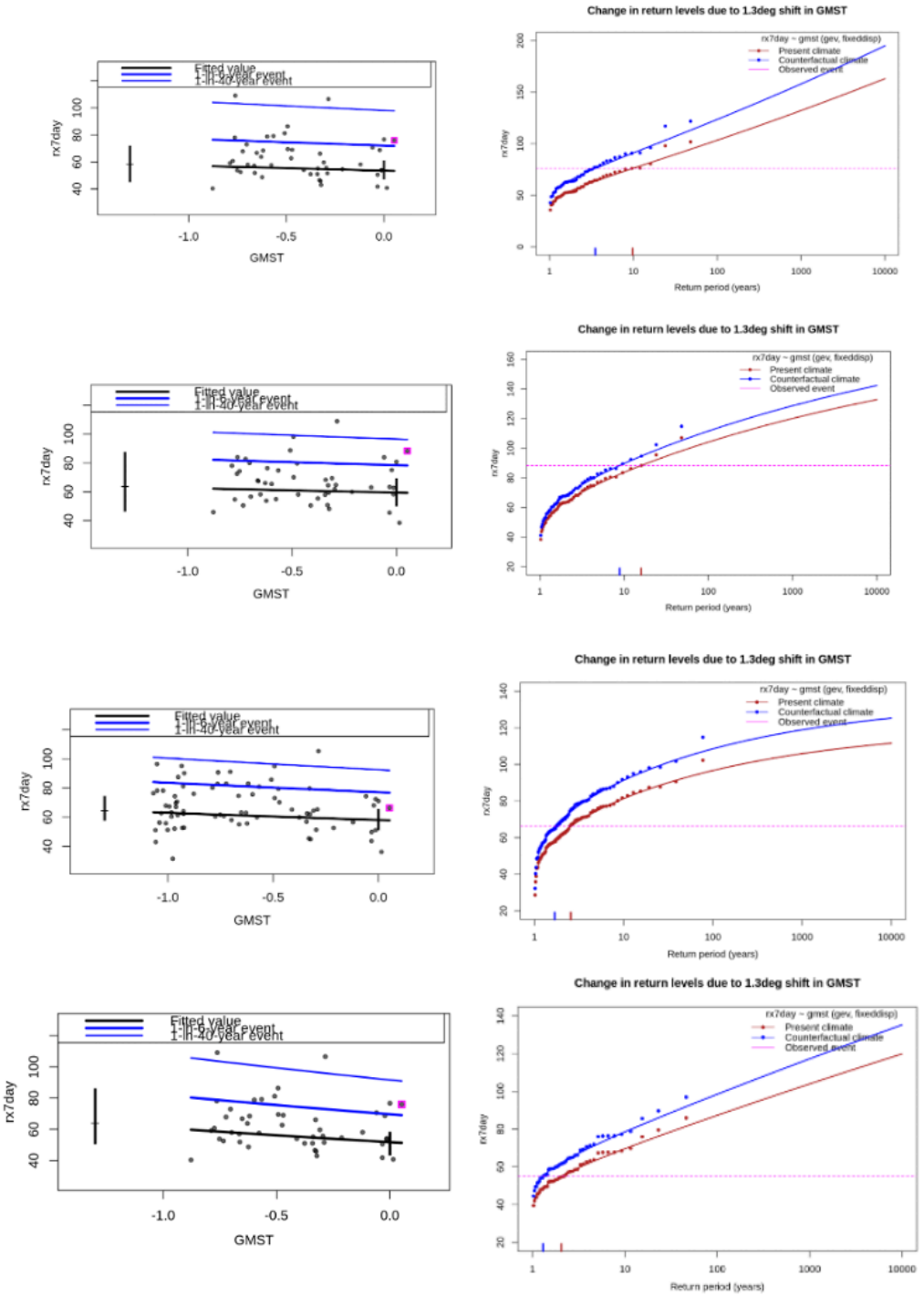

Figure A2: *GEV fit with fixed dispersion and location parameter scaling proportional to GMST of the index series.* ***(left)*** *Observed annual (Jul-June) max.7-day cumulative rainfall [mm/7day] as a function of the smoothed GMST. The thick red line denotes the time-varying location parameter. The vertical red lines show the 95% confidence interval for the location parameter, for the current, 2025 climate and the fictional, 1.3ºC cooler climate. The 2025 observation is highlighted with the magenta box.* ***(right)*** *Return time plots for the climate of 2025 (red) and a climate with GMST 1.2 ºC cooler (blue). The past observations are shown twice: once shifted up to the current climate and once shifted down to the climate of the pre-industrial era. The markers show the data and the lines show the fits and uncertainty from the bootstrap. The magenta line shows the magnitude of the 2025 event analysed*

here. These are shown for MSWEP (top), CPC (second row), ERA5 (third row) and CHIRPS (bottom), For the CHIRPS dataset, the magnitude of the 1-in-50 year event is highlighted by the magenta box.

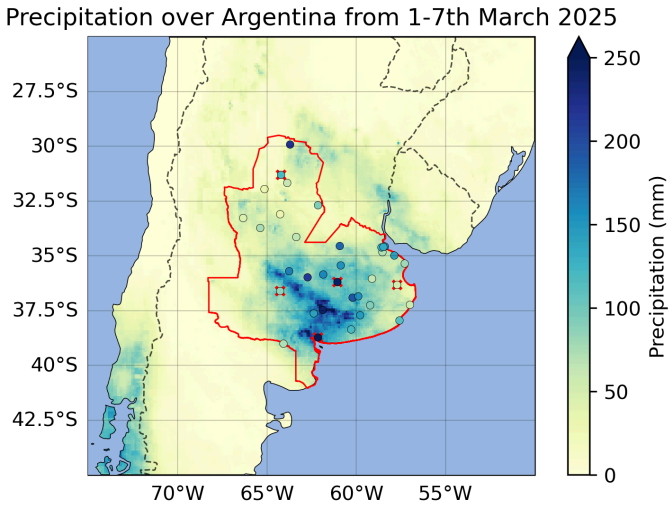

Figure A3: 7-day accumulated rainfall during 1-7 March 2025, based on MSWEP data. The study region is highlighted in red. The scatter plots show the rainfall accumulations for the same period from 25 weather stations by the National Weather Service of Argentina (NWS). The red highlights in the scatter plots correspond to Bahía Blanca, Dolores, Santa Rosa, Bolívar and Córdoba stations.

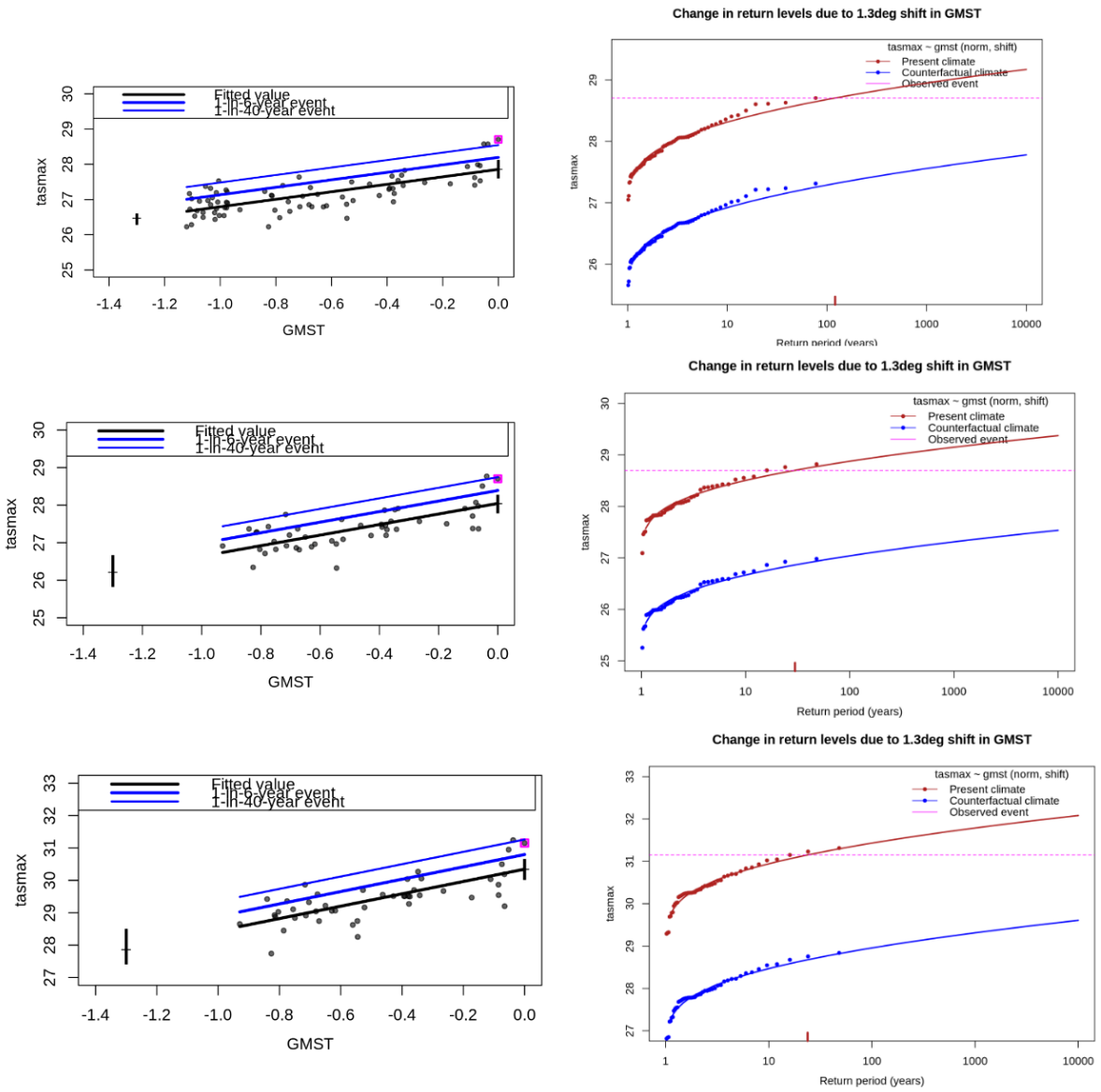

Figure A4: GEV fit with scale and shape parameter scaling proportional to GMST of the index series TMaxDJFM over the study region to change in global mean temperature. (left) The thick black line denotes the time-varying mean, and the thin red lines show 1 standard deviation (s.d) and 2 s.d above. The vertical red lines show the 95% confidence interval for the location parameter, for the current, 2024/25 climate and the hypothetical, 1.3ºC cooler climate. The 2025 event is highlighted with the magenta box, and (right) Return periods for the 2024/25 climate (red lines) and the 1.3ºC cooler climate (blue lines with 95% CI), based on (top) ERA5 (b) MSWEX and (c) CPC datasets.

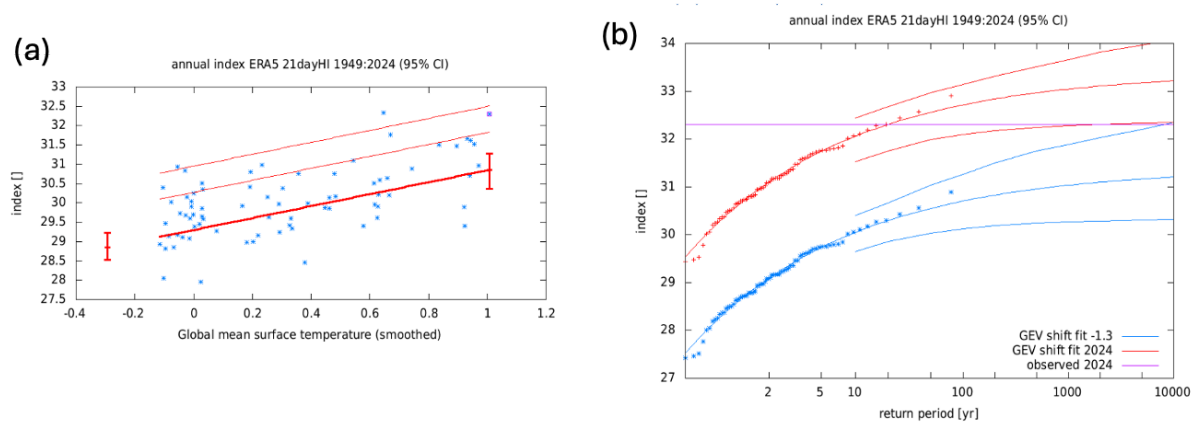

Figure A5: GEV fit with scale and shape parameter scaling proportional to GMST of the index series HIx21day over the study region estimated from ERA5 records to change in global mean temperature. The thick red line denotes the time-varying mean, and the thin red lines show 1 standard deviation (s.d) and 2 s.d above. The vertical red lines show the 95% confidence interval for the location parameter, for the current, 2024/25 climate and the hypothetical, 1.3℃ cooler climate. The 2025 event is highlighted with the magenta box. Bottom right: Return periods for the 2024/25 climate (red lines) and the 1.3℃ cooler climate (blue lines with 95% CI), based on ERA5 data.

Table A1: Estimated return periods of RX7day at 5 locations in the study region, based on the NWS station data, along with the Probability ratio and the change in magnitude for RX7day both due to GMST. Trends that are statistically significant are highlighted in bold text.

Dataset	Event		Trend	
	Magnitude	Return period	PR	Change in intensity
Bahía Blanca	324.8	540.4 (60.91 - inf)	1.57 (10^{-5} - 284.81)	7.64 (-27.15 - 60.84)
Dolores	73.1	1.06 (1.01 - 1.20)	1.09 (0.91 - 1.26)	22.99 (-19.51 - 72.16)
Santa Rosa	85.8	1.16 (1.03 - 1.43)	**1.58** **(1.02 - 2.42)**	**34.7** **(1.22 - 76.79)**
Bolívar	243	12.66 (3.62 - 74.78)	1.86 (0.16 - inf)	14.94 (-39.27 - 117.48)
Córdoba	205	18.32 (6.10 - 569.30)	2.05 (0.14 - 54.47)	9.86 (-18.09 - 39.96)